

Modeling impacts of dust mineralogy on fast climate response

1
2
3
4
5
6
7
8
9
10
11
12
13

Qianqian Song¹, Paul Ginoux², María Gonçalves Ageitos^{3,4}, Ron L. Miller^{5,6}, Vincenzo Obiso⁵,
Carlos Pérez García-Pando^{4,7}

¹ Atmospheric and Oceanic Sciences Program, Princeton University, Princeton, NJ, USA

² NOAA Geophysical Fluid Dynamics Laboratory, Princeton, NJ, USA

³ Projects and Construction Engineering Department. Universitat Politècnica de Catalunya-Barcelona
TECH, Terrassa, Spain

⁴ Barcelona Supercomputing Center, Barcelona, Spain

⁵ NASA Goddard Institute for Space Studies, New York, NY, USA

⁶ Department of Applied Physics and Applied Mathematics, Columbia University, New York, NY, USA

⁷ ICREA, Catalan Institution for Research and Advanced Studies, Barcelona, Spain

Correspondence: Qianqian Song (qs7080@princeton.edu)

14 **Abstract**

15 Mineralogical composition drives dust impacts on Earth's climate systems. However, most climate
16 models still use homogeneous dust, without accounting for the temporal and spatial variation in
17 mineralogy. To quantify the radiative impact of resolving dust mineralogy on Earth's climate, we
18 implement and simulate the distribution of dust minerals (i.e., illite, kaolinite, smectite, hematite,
19 calcite, feldspar, quartz, and gypsum) from Claquin et al. (1999) (C1999) and activate their
20 interaction with radiation in the GFDL AM4.0 model. Resolving mineralogy reduces dust
21 absorption compared to the homogeneous dust used in the standard GFDL AM4.0 model that
22 assumes a globally uniform hematite volume content of 2.7% (HD27). The reduction in dust
23 absorption results in improved agreement with observation-based single scattering albedo (SSA),
24 radiative fluxes from CERES (the Clouds and the Earth's Radiant Energy System), and land
25 surface temperature from CRU (Climatic Research Unit), compared to the baseline HD27 model
26 version. It also results in distinct radiative impacts on Earth's climate over North Africa. Over the
27 19-year (from 2001 to 2019) modeled period during JJA (June-July-August), the reduction in dust
28 absorption in AM4.0 leads to a reduction of over 50% in net downward radiation across the Sahara
29 and approximately 20% over the Sahel at top of atmosphere (TOA) compared to the baseline HD27
30 model version. The reduced dust absorption weakens the atmospheric warming effect of dust
31 aerosols and leads to an alteration in land surface temperature, resulting in a decrease of 0.66 K
32 over the Sahara and an increase of 0.7 K over the Sahel. The less warming in the atmosphere
33 suppresses ascent and weakens the monsoon inflow from the Gulf of Guinea. This brings less
34 moisture to the Sahel, which combined with decreased ascent induces a reduction of precipitation.
35 To isolate the effect of reduced absorption, compared to resolving spatial and temporal mineralogy,
36 we carry out a simulation where the hematite volume content of homogeneous dust is reduced
37 from 2.7% to 0.9% (HD09). The dust absorption (e.g., single scattering albedo) of HD09 is
38 comparable to that of the mineralogically speciated model on a global mean scale, albeit with a
39 lower spatial variation that arises solely from particle size. Comparison of the two models indicates
40 that the spatial inhomogeneity in dust absorption resulting from resolving mineralogy does not
41 have significant impacts on Earth's radiation and climate, provided there is a similar level of dust
42 absorption on a global mean scale before and after resolving dust mineralogy. However,
43 uncertainties related to emission and distribution of minerals may blur the advantages of resolving
44 minerals to study their impact on radiation, cloud properties, ocean biogeochemistry, air quality,

45 and photochemistry. On the other hand, lumping together clay minerals (i.e., illite, kaolinite, and
46 smectite), but excluding externally mixed hematite and gypsum, appears to provide both
47 computational efficiency and relative accuracy. Nevertheless, for specific research, it may be
48 necessary to fully resolve mineralogy to achieve accuracy.

49 **1 Introduction**

50 Soil dust aerosols emitted from erodible land surfaces, hereafter referred to as dust, are the most
51 abundant aerosol component in the atmosphere in terms of dry mass. Dust has significant impacts on
52 the Earth's climate systems (atmosphere, ocean, cryosphere) due to its interaction with terrestrial and
53 solar radiation (Sokolik and Toon, 1999), cloud microphysics (Guo et al., 2021), tropospheric
54 chemistry (Bian and Zender, 2003; Paulot et al., 2016), and oceanic and terrestrial
55 biogeochemistry (Mahowald, 2011; Evans et al., 2019; Dunne et al., 2020). In addition, dust particles
56 deposited on snow and ice decrease surface reflectivity and accelerate snowmelt (Skiles et al., 2018;
57 Réveillet et al., 2022). Dust can influence Earth's radiative energy budget through different pathways;
58 among them: 1) directly by interacting with both solar and terrestrial radiation (i.e., direct radiative
59 effects, hereafter referred to as DRE) 2) by radiatively influencing the thermal dynamical structure of
60 atmosphere and thereby clouds (i.e., semi-direct radiative effect) and 3) indirectly by altering cloud
61 reflectivity (cloud albedo effect) and lifetime (cloud lifetime effect). Unfortunately, the quantitative
62 estimate of dust DRE at the top of atmosphere (TOA) is largely uncertain (Claquin et al., 1998; Miller
63 et al., 2014; Kok et al., 2017; Song et al., 2022). A significant part of this uncertainty has been attributed
64 to neglecting variations in dust mineralogical composition and its evolution during transport (Li et al.,
65 2021).

66 The magnitude of dust impacts on the Earth's climate systems depends on its mineralogical
67 composition, as has been shown in multiple studies. In the ShortWave (SW), dust absorption depends
68 on the iron oxides content. Sokolik and Toon (1999) suggested that a small amount of iron oxides
69 internally mixed with less absorptive minerals is able to reverse the sign of DRE_{SW} at TOA from
70 negative (cooling effect) to positive (warming effect). Multiple studies have confirmed the importance
71 of iron oxides to the dust DRE_{SW} (Balkanski et al., 2007; Li et al., 2021; Obiso et al., 2023). In
72 LongWave (LW) spectrum, absorption and DRE_{LW} depend on the abundance of quartz, calcite, and
73 clays in coarse and super-coarse modes (Di Biagio et al., 2017; Sokolik and Toon, 1999). As a result,
74 resolving dust mineralogy allows to better understand the impact of dust DRE, such as the fast response
75 of the land surface temperature, as opposed to the slow response of sea surface temperature that will

76 not be studied here. This fast temperature response will affect precipitation, and atmospheric
77 circulation (Ming et al., 2010; Persad et al., 2014).

78 In addition, resolving dust mineralogy is also crucial for studying heterogeneous reactions of acid gases
79 with dust aerosols. For example, the uptake of HNO_3 , NO_3^- , N_2O_5 on dust particles is suggested to be
80 limited by alkalinity that comprises calcium and magnesium carbonates (Song and Carmichael, 2001;
81 Paulot et al., 2016). These reactions will modify the composition of dust particles and subsequently
82 changing their hygroscopicity, cloud condensation nucleation (CCN), and ice nucleation activities
83 (Kelly et al., 2007), and thereby further affecting precipitation (Rosenfeld et al., 2001). Moreover,
84 heterogeneous reactions with mineral dust could significantly affect tropospheric photochemical
85 oxidation cycles, causing up to 10% reduction in O_3 concentrations in dust source regions and nearby
86 (Dentener et al., 1996). Among the different minerals, K-Feldspar appears to dominate ice nucleation,
87 despite being a minor component of aeolian dust (Atkinson et al., 2013; Harrison et al., 2019), although
88 other minerals such as quartz may also contribute (Chatziparaschos et al., 2023). The key factor
89 controlling the production and removal of pollutants and the damages by acid rain is the pH of
90 raindrops, which has been observed to increase due to its dependency on Ca-rich dust (Grider et al.,
91 2023).

92 Despite the potential importance of resolving dust mineralogy in various aspects, current climate
93 models tend to use a fixed mineralogy without considering the temporal and spatial variations in
94 dust mineralogical composition. To test the importance of resolving dust mineralogy on the fast
95 climate response (e.g., surface temperature response over land, atmospheric circulation and
96 precipitation response) through its interactions with SW and LW radiation (i.e., through dust DRE),
97 dust mineralogy has been implemented and simulated in the GFDL AM4.0 model (Zhao et al.,
98 2018a, b), including its on-line interactions with radiation. Following the pioneering work of
99 Claquin et al. (1999) (C1999), we consider the emission, transport and interactions with radiation
100 and deposition of eight minerals: illite, kaolinite, smectite, hematite, calcite, feldspar, quartz and
101 gypsum. Following the recent launch of the Earth Surface Mineral Dust Source Investigation
102 (EMIT) instrument specifically designed to retrieve global distribution of dust mineralogy over
103 dust sources (Green et al., 2020), there have been coordinated efforts to represent dust mineralogy
104 and investigate DRE of mineral-speciated dust in climate models, in particular in Li et al. (2021),
105 Gonçalves Ageitos et al. (2023), and Obiso et al. (2023). However, to the best of our knowledge,
106 there have been no studies investigating the fast climate impact of dust while accounting for its

107 mineral speciation. Our work contributes to these efforts by incorporating dust mineralogy into the
108 GFDL models, and it is distinguished by extending its investigation to the fast climate response of
109 mineral-specified dust. The impacts of dust mineralogy on other aspects, such as sea surface
110 temperature and slow climate response, heterogeneous reactions, and ice nucleation ability, will
111 be examined in future studies.

112 Section 2 provides the description of the GFDL AM4.0 model and dust mineralogy
113 implementation. Section 3 describes our experimental design. In Section 4, we calculate mineral
114 optical properties, activate the interaction of minerals with radiation in GFDL AM4.0 and compare
115 modeled dust optical properties with observations. Section 5 presents the impacts of resolving dust
116 mineralogy on Earth's radiation and climate with a focus on the North Africa, as well as their
117 evaluations. In Section 6, we investigate the influences of reducing the number of mineral tracers.
118 Section 7 provides a summary of the study along with the main conclusions.

119 **2 Model and Data**

120 **2.1 Model description**

121 We conduct a series of experiments with GFDL AM4.0 (Zhao et al., 2018a, b) over the period
122 2001-2019. These experiments use the AMIP protocol, where sea surface temperature (SST) and
123 sea-ice are imposed based upon average monthly observations (see Gates, 1992 for details) .
124 Observed gridded SST and sea-ice concentration boundary conditions are from the reconstructions
125 of Taylor et al., (2000). Historical reconstructions of monthly solar spectral irradiances are from
126 Matthes et al., (2017). For radiation calculations, global monthly mean concentrations of
127 greenhouse gases (GHGs), including nitrous oxide (N₂O), and ozone-depleting substances (ODSs,
128 including CFC-11, CFC-12, CFC-113, and HCFC-22) are specified from Meinshausen et al.,
129 (2017). The solar irradiances and GHG databases are standard for CMIP6. Longwave (LW)
130 scattering of aerosols is not accounted for in the model.

131 In AM4.0, dust emission is calculated interactively following the parameterization of Ginoux et al.
132 (2001) with a threshold of wind erosion and global scaling factor of 3.5 m s^{-1} and $0.2 \mu\text{g s}^2 \text{ m}^{-5}$,
133 respectively. Dust size is represented by five bins with diameter ranging from $0.2 \mu\text{m}$ to $20 \mu\text{m}$
134 (bin1: $0.2 - 2 \mu\text{m}$, bin2: $2 - 3.6 \mu\text{m}$, bin3: $3.6 - 6 \mu\text{m}$, bin4: $6 - 12 \mu\text{m}$, bin5: $12 - 20 \mu\text{m}$). The

135 corresponding source fractions have been updated from 0.1, 0.225, 0.225, 0.225 and 0.225 to
136 values of 0.04, 0.14, 0.19, 0.49, and 0.14 for the five bins. These updated source functions allocate
137 more fraction to coarser size bins, following the suggested Brittle Fragmentation Theory (BFT) as
138 proposed by Kok et al. (2011). Dust mineral composition in the standard AM4.0 is considered as
139 uniform, with no temporal and spatial variations; in other words, dust Refractive Index (RI) is
140 temporally and spatially homogeneous (case referred to as homogeneous dust hereafter). The dust
141 RI in the standard AM4.0 is taken from Balkanski et al., (2007), assuming a fixed hematite content
142 of 2.7% by volume (HD27), which was calculated for the internal mixture of hematite and five
143 other minerals (calcite, quartz, illite, kaolinite and montmorillonite) using the Maxwell Garnett
144 mixing rule (see details in Balkanski et al., 2007). The decision to fix the hematite content for dust
145 particles at 2.7% was made during the development of the previous GFDL Climate Model CM3
146 (Donner et al., 2011). This decision was prompted by the discovery that dust absorption was
147 unrealistically high (by a factor 3) in CM2 (Delworth et al., 2006) compared to AERONET
148 observations (Balkanski et al., 2007). In CM3, the conjunction of a sharp decrease of black carbon
149 (strong aerosol absorber) with a new emission inventory and the switch to more scattering dust
150 had a negative effect on precipitation bias, and late 20th century warming (see Donner et al., 2011
151 for details). To mitigate this bias, the selection of 2.7% hematite was adopted in CM3, as well as
152 in the subsequent GFDL models. The control run conducted with the homogeneous dust in the
153 standard AM4.0 model is labeled as HD27 as described in Table 2.

154 In addition, we conduct simulations assuming homogeneous dust with hematite content of 0.9%
155 by volume, with RI from Balkanski et al. (2007). Similar to HD27, this experiment, labeled as
156 HD09 in Table 2, does not account for the temporal and spatial variations in dust mineralogy.

157 **2.2 Dust mineralogy implementation**

158 Claquin et al. (1999) (C1999) is the earliest study providing a soil mineralogy map oriented toward
159 atmospheric and climate modelling. The soil map provides the mineral mass fractions present in
160 the clay and silt size ranges for eight different minerals, namely: illite, smectite, kaolinite, calcite,
161 quartz, feldspars, gypsum, and hematite. In this study, we implement the eight minerals from the
162 soil mineralogy map provided by C1999 in GFDL AM4.0 to resolve dust mineralogy. The soil
163 map is based on soil analyses that are usually done after wet sieving, which disperse mineral
164 aggregates into small particles. This dispersal is particularly relevant for the phyllosilicates,

165 typically found in the form of aggregates in soils. They are detected in the atmosphere with higher
166 proportions at coarser (silt) sizes than those reported in the soil maps (Perlwitz et al., 2015b; Perez
167 Garcia-Pando et al., 2016). These recent studies also show that the Brittle Fragmentation Theory
168 (BFT; Kok, 2011) represents a practical framework to generate the emitted particle size
169 distribution based on the dispersed soil PSD, which facilitates the utilization of soil mineralogy
170 maps. In our simulations, we employ BFT to reconstruct the mineral aggregates emitted from the
171 original undispersed soils, following the methods described in Gonçalves Ageitos et al., 2023. The
172 mass density of the eight minerals, along with a brief description of their importance to Earth's
173 climate, are listed in Table 1. The density of minerals impacts their settling velocity, which is
174 relevant to the removal of particles in the atmosphere. Goethite and hematite are the two major
175 types of iron oxides present in soils. Goethite is less absorptive than hematite and is not resolved
176 in C1999. So, iron oxides are represented by hematite in this study. Hematite has larger density
177 than other minerals, so that hematite deposits more quickly and is not able to be transported to
178 remote regions when not aggregated or internally mixed with lighter clay minerals. Moreover,
179 among the minerals considered here, hematite is the strongest absorber at ultraviolet (UV) and
180 visible wavelengths, while it does not have noticeable absorption at infrared wavelengths (IR)
181 compared to other minerals (Sokolik and Toon, 1999). As such, the correct representation of
182 hematite content in dust aerosols is critical in improving the representation of dust interaction with
183 SW radiation in climate models. All minerals are considered to be externally mixed, except for
184 iron oxides. A large part of the emitted flux of iron oxides is considered to be internally mixed
185 with other minerals, e.g., in the form of accretions in phyllosilicates, in line with observational
186 evidence and previous modeling studies (Kandler et al., 2009; Perlwitz et al., 2015a; Zhang et al.,
187 2015; Panta et al., 2023). As suggested by Gonçalves Ageitos et al. (2023), we define two different
188 types of tracers for the iron oxides: one set of tracers carries the mass of the hematite that
189 constitutes small accretions in clay minerals (i.e., internally mixed with clay minerals), are allowed
190 to be up to 5 % of the masses of their host minerals at emission (Perlwitz et al., 2015a; Gonçalves
191 Ageitos et al., 2023). Given the low fractional mass of hematite compared to their host minerals,
192 we assume that these accretions do not change the density of their host particles. These internally
193 mixed accretions form the largest fraction of the emitted hematite. Another smaller set of tracers
194 carries the mass of the remaining fraction of hematite, which is considered to be externally mixed
195 with the other minerals, including the internal mixtures of hematite with clay.

196 In addition to the similar roles of clay minerals in carrying iron oxides, the optical properties of
197 the three clay minerals are very similar, and the optical properties of their external mixture are
198 found to be almost identical to their internal mixture (see Section S1 in the Supplement). This
199 finding suggests the use of a single mineral species to represent all three clay minerals in their
200 interaction with radiation to reduce computational cost. Therefore, the optical properties of one
201 single mineral (clay433) are used to represent the optical properties of all three clay minerals. The
202 clay433 represents a mixed mineral comprising three clay minerals: illite, kaolinite and smectite,
203 with mass fraction of 40%, 30%, and 30%, respectively (see detailed descriptions in
204 Supplementary Section S1). This simplification streamlines the calculations of optical properties
205 for internal mixtures of hematite and the three clay minerals (illite, kaolinite, and smectite),
206 reducing it from an internal mixture of four minerals (hematite, illite, kaolinite and smectite) to an
207 internal mixture of two minerals (hematite and clay433).

208 The optical properties of the internal mixture of hematite and clay433 are calculated using three
209 mixing rules: volume weighted average (VOL-mixing), Maxwell-Garnett mixing rule (MG-
210 mixing) and Bruggeman mixing rule (BM-mixing). Generally, VOL-mixing is used for a quasi-
211 homogeneous mixture, that is when the components have similar refractive index. For cases
212 involving dominant homogeneous host with small inclusions of contrasting composition, MG-
213 mixing is appropriate. BM-mixing is suitable for mixtures that the inclusions virtually occupy the
214 entire volume of the particle, and the host disappears. The detailed discussion regarding the three
215 mixing rules and their applications can be found in Liu and Daum (2008) and Markel (2016). The
216 appropriate selection of mixing rules is important for the determination of the optical properties of
217 the mixtures. Therefore, we incorporate all three mixing rules in this study. These calculations are
218 performed for various volume mixing fractions of hematite with respect to clay433, to construct a
219 lookup table (LUT) for each mixing rule. The optical properties of each mineral as well as the
220 internal mixtures of hematite and clay433 are calculated offline using Mie code with a spherical
221 shape assumption. As all other minerals have similar SW absorption, internal or external mixing
222 does not change their absorption properties. So, we assume all other minerals to be externally
223 mixed. More details about optical properties of minerals will be discussed in Section 4.

224 Overall, we implement nine types of mineral tracers: seven non-hematite minerals along with
225 distinguished internal and external hematite, as listed in Table 1. Each type is distributed across

226 five size bins. As a result, 45 mineral tracers have been incorporated in AM4.0 to account for dust
 227 mineralogy.

228 Table 1. The list of minerals considered in this study and their importance to Earth’s climate. Mineral-
 229 dependent mass densities are defined following Table 1 in Gonçalves Ageitos et al. (2023), in which the
 230 references of mineral densities are listed.

Minerals	Density (kg/m³)	Importance
1. Hematite (int.)	2570	It is the strongest visible absorber. It is internally mixed with clay minerals when its mass fraction at emission < 5%.
2. Hematite (ext.)	4770 ⁽¹⁾	It is externally mixed for the part of emitted mass fraction > 5%.
Three clay minerals: 3. Illite 4. Smectite 5. Kaolinite Clay in BM-RT	2570 2570 2630 2590	They are the most abundant mineral components in clay-sized (diameter < 2 μ m) minerals. They are internally mixed with internal hematite. The three clay minerals are lumped together as one mineral species ‘clay’ in the BM-RT experiment in Section 6.
6. Calcite	2710	It is important for chemistry. (e.g., heterogeneous reaction with acidic gases and formation of sulfate and nitrates on the surface of dust particles, and cloud droplet pH)
7. Feldspar	2680	A fraction of feldspar (K-feldspar) is important for ice nucleation
8. Quartz	2670	It is the most abundant mineral component in silt-sized (diameter:2-63 μ m) minerals. It is important for LW absorption and ice nucleation.
9. Gypsum	2308	It possibly has impact on chemistry, but the impact is likely unimportant given the low abundance globally.

⁽¹⁾ We use the mean of hematite and goethite densities for hematite, as in Gonçalves Ageitos et al. (2023).

231 **2.3 AERONET Dust SSA**

232 The AERONET Version 3 Level 2.0 Almuqantar inversion retrievals (Giles et al., 2019; Sinyuk et
 233 al., 2020) from 2000 to 2020 are screened for dust events following the methodology in Gonçalves
 234 Ageitos et al. (2023) and Obiso et al. (2023). This screening process aims to select dust-dominated
 235 events and filter out the AERONET scenes contaminated by other absorbing aerosols. The criteria
 236 that are applied to AERONET retrievals to screen dust events are: 1) hourly retrievals from
 237 AERONET are considered to represent dust when the fine volume fraction is small (below 15%),
 238 2) the SSA increases from 440 nm to 675 nm (a feature that distinguishes dust from other species,
 239 see Dubovik et al., 2002), and 3) the mean of the imaginary index at red and near-infrared

240 wavelengths (675, 870 and 1020 nm) is lower than 0.0042 (as higher values would indicate the
241 presence of absorbing black and brown carbon, following Schuster et al., 2016). We calculate
242 AERONET SSA in the visible by averaging AERONET retrieved SSA at two visible wavelengths
243 (0.44 μm and 0.67 μm) weighted by solar spectrum following Eq. (2).

244 **2.4 Laboratory Dust SSA**

245 The lab measured dust SSA at 550 nm is obtained from Di Biagio et al. (2019) (DB-2019 hereafter),
246 in which dust SSA was directly retrieved from scattering and absorption measurements. We
247 acknowledge the limits of laboratory measurements, where the dust samples are not aerosols
248 present in the atmosphere, but instead are reemitted in the lab from soil samples collected from
249 various source regions. Consequently, the laboratory measurements in DB-2019 do not account
250 for dust aerosols transported from other regions to the regions of interest. In addition, in contrast
251 to the modeled dust diameter range of 0.2 μm to 20 μm , DB-2019 measures dust particles with a
252 diameter ranging from 0.2 μm up to 10 μm .

253 **2.5 CERES Data**

254 To compare modeled fluxes at TOA with observations, we use the Clouds and the Earth's Radiant
255 Energy System (CERES) Energy Balanced and Filled (EBAF) Edition-4.2 data (Loeb et al., 2018).
256 The standard CERES level-3 products provide clear-sky fluxes by averaging all CERES footprints
257 within a region that are completely free of clouds. Therefore, there are many missing regions in
258 monthly mean clear-sky TOA flux maps because completely cloud-free conditions are not always
259 observed at the CERES footprint scale (~ 20 km at nadir). In contrast to the standard CERES level-
260 3 products, CERES_EBAF product infers clear-sky fluxes from clear portions of partly cloudy
261 CERES footprints thereby producing a clear-sky TOA flux climatology free of any missing regions
262 (details in Loeb et al., 2018). Starting from CERES_EBAF_Ed4.1, the product also provides clear-
263 sky flux estimates for the total region (i.e., the total CERES footprints) by combining CERES
264 observations and radiative transfer calculations, which represents clear-sky flux with clouds
265 removed from the entire atmospheric column of CERES footprints. These clear-sky fluxes for the
266 total region are defined in a way that is more consistent with how clear-sky fluxes are represented
267 in climate models (for details see CERES_EBAF_Ed4.1 Data Quality Summary). In this study,
268 the monthly mean TOA 'Clear-Sky Flux Estimate for Total Region' variables in the
269 CERES_EBAF_Ed4.2 product, the most recent version of the product, are used to compare with

270 modeled monthly mean clear-sky flux at TOA. The comparisons allow us to examine the
 271 agreement of modeled clear-sky fluxes from different experiments with observations. The
 272 comparison results will be shown in section 5.1.

273 **2.6 CRU TS Data**

274 The CRU TS (Climatic Research Unit gridded Time Series) dataset provides high-resolution (0.5°
 275 latitude × 0.5° longitude) climate dataset over land except Antarctica. The dataset is based on
 276 extensive networks of weather stations going back to 1901(Harris et al., 2020). This dataset has
 277 been widely used in various research areas since its first release in 2000. The mean 2-meter
 278 temperature (TMP) and precipitation rate (PRE) variables from CRU TS v4.07 are used to evaluate
 279 our model simulations. The results will be shown in section 5.2 and section 5.3.

280 **3 Experimental Design**

281 Table 2. List of experiments and their description. Experiments are named based on the type of dust used
 282 or the mixing rules for minerals applied in each experiment.

Experiments	Dust or Minerals	Description	Optics
HD27	HD27	Dust refractive index is spatially and temporally uniform. Dust is assumed to contain 2.7% of hematite by volume. Its optical properties are used to represent dust in the standard GFDL AM4.0 model.	Balkanski et al. (2007)
HD09	HD09	Dust refractive index is spatially and temporally uniform. Dust is assumed to contain 0.9% of hematite by volume.	Balkanski et al. (2007)
VOL	VOL-mixing	Soil mineralogy from C1999 is implemented in AM4.0. Hematite (int.) is internally mixed with clay minerals following the volume-weighted mean mixing rule.	Scanza et al. (2015)
MG	MG-mixing	Soil mineralogy from C1999 is implemented in AM4.0. Hematite (int.) is internally mixed with clay minerals following the Maxwell Garnett mixing rule.	Scanza et al. (2015)
BM	BM-mixing	Soil mineralogy from C1999 is implemented in AM4.0. Hematite (int.) is internally mixed with clay minerals following the Bruggeman mixing rule.	Scanza et al. (2015)
BM-RT	BM-mixing	Three experiments are performed step by step to reduce the number of mineral tracers. 1) BM-LC experiment: following BM experiment, illite, kaolinite and smectite are lumped together as one tracer ‘clay’.	Scanza et al. (2015)

		2) BM-LCRH experiment: following BM-LC, the tracer of external mixed hematite is removed, its mass is combined with internal mixed hematite. 3) BM-LCRHRG experiment: following BM-LCRH, gypsum tracer is removed, and its mass is proportionally added to all other remaining minerals.	
--	--	---	--

283 We conduct a total of six experiments using the GFDL AM4.0 model, with each experiment's
 284 description provided in Table 2. Two of these experiments serve as control runs in which dust
 285 aerosols are represented with temporally and spatially fixed composition in the model. The first
 286 control run, referred to as HD27, represents how dust aerosols are implemented in the standard
 287 GFDL AM4.0 model (Zhao et al., 2018a). The second control run is the HD09, in which dust is
 288 more scattering than that in the standard AM4.0 model (i.e., HD27) due to its reduced hematite
 289 volume fraction from 2.7% to 0.9%.

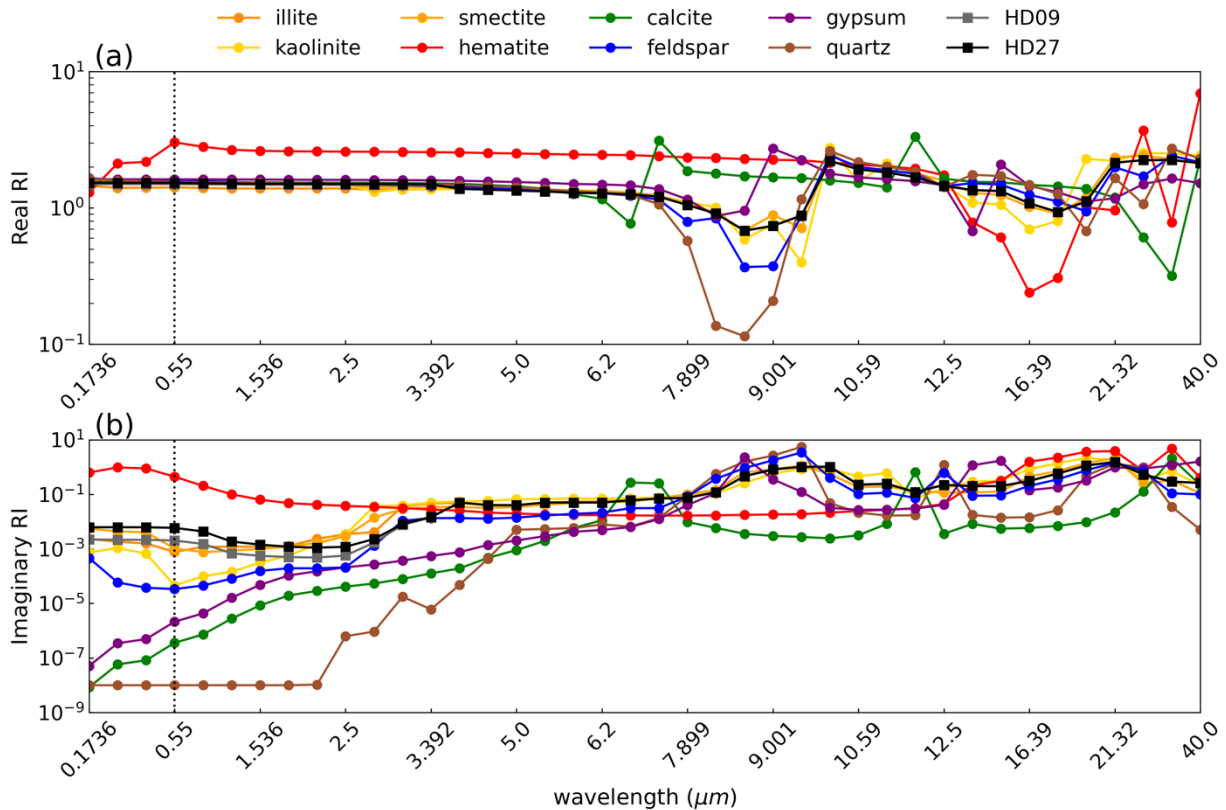
290 The other three experiments, namely VOL, MG, and BM, resolve dust mineralogy and activate
 291 their interaction with radiation. These three experiments incorporate 45 mineral tracers for nine
 292 types of mineral tracers distributed over five size bins as described in Section 2.2. Additionally,
 293 we conduct the BM-RT experiments, which consist of three sub-experiments: BM-LC, BM-LCRH,
 294 BM-LCRHRG. These experiments aim to explore the potential of reducing mineral tracers, which
 295 can improve the model computational efficiency. The results will be discussed in Section 6.

296 Each of the experiments ran for 19 years, from 2001 to 2019. We consider the 19-year runs of the
 297 experiment as a group of simulations, containing 19 members of one-year simulation. The two
 298 control runs (i.e., HD27 and HD09), combined with the three mineral-resolved experiments (i.e.,
 299 VOL, MG, and BM), form a total of six contrasting pairs. In this study, for each contrasting pair,
 300 we define the anomaly as the group mean difference (based on 19-year mean) between mineral-
 301 resolved experiment and control run. An anomaly is considered statistically significant if the p-
 302 value, determined by the student's t-test between the two contrasting groups of simulations, is
 303 smaller than 0.05.

304 **4 Optical Properties**

305 **4.1 Dust optical properties**

306



307

308 Figure 1. Real part and imaginary part of complex refractive indices (RI) of two homogeneous dust (e.g.,
 309 HD27 and HD09) and eight minerals (Scanza et al., 2015). The dotted lines represent the real part (a) and
 310 imaginary part (b) of dust or minerals for the corresponding wavelength. The black and grey dotted lines
 311 are for HD27 and HD09, respectively. The colorful dotted lines are for the eight minerals.

312 We use the refractive indices (RI) of each mineral from Scanza et al. (2015) and the RI of HD27
 313 and HD09 from Balkanski et al. (2007) to calculate the LUT of optical properties. The spectral RI
 314 of each mineral and homogeneous dust (e.g., HD27 and HD09) are shown in Figure 1. The HD09
 315 dust has lower imaginary part of RI at 550 nm than HD27 dust, indicating its lower absorption in
 316 the visible band due to a reduced content of hematite.

317 After calculating LUT of optical properties (details in Section 2.2), we incorporate the interaction
 318 of minerals with radiation into GFDL AM4.0. The modeled emission, load, deposition, and
 319 lifetime for each mineral are provided in Table S1 in the Supplement. Table 3 provides global
 320 total dust emission, load, globally averaged dust aerosol optical depth (DAOD) and SSA for each
 321 experiment listed in Table 2 and their comparisons with previous studies. DAOD and SSA from
 322 AM4.0 simulations are averaged in the visible band (0.44 - 0.625 μm) of GFDL AM4.0. Unless
 323 otherwise specified, DAOD and SSA in this study refer to the average in the visible band. Note

324 that in our calculations, the domain averaged DAOD is always weighted by the area of each grid
 325 cell. The domain averaged SSA is always weighted by the area and DAOD of each grid cell.
 326 Additionally, the spectrally averaged DAOD and SSA are always weighted by the TOA solar
 327 radiation intensity at the corresponding wavelengths, peaking around 0.50 μm , as shown in Eq. (1)
 328 and Eq. (2).

$$\overline{DAOD} = \frac{\int_{\lambda_1}^{\lambda_2} DAOD(\lambda) B(\lambda) d\lambda}{\int_{\lambda_1}^{\lambda_2} B(\lambda) d\lambda} \quad \text{Eq. (1)}$$

$$\overline{SSA} = \frac{\int_{\lambda_1}^{\lambda_2} SSA(\lambda) DAOD(\lambda) B(\lambda) d\lambda}{\int_{\lambda_1}^{\lambda_2} B(\lambda) DAOD(\lambda) d\lambda} \quad \text{Eq. (2)}$$

329 Where $B(\lambda)$ describes the solar radiation energy intensity, which can be calculated by means of
 330 the Planck's function $B(T, \lambda)$, using the temperature of the Sun ($T = 5800 \text{ K}$).

331 Table 3. 19-year (2001-2019) averaged global dust emission, load, globally averaged visible band dust
 332 optical depth (\overline{DAOD}) and single scattering albedo (\overline{SSA}) for each experiment in this study. We use each
 333 grid-cell surface area as a weight for the global DAOD average. We use each grid-cell surface area times
 334 DAOD in each grid-cell as a weight for the global SSA average. In addition, we include the results from
 335 previous studies for the purpose of comparison. Note, the modeled DAOD and SSA in this study are
 336 averaged in the visible band (0.44 - 0.625 μm) of GFDL AM4.0, while averaged in the UV-VIS band (0.30
 337 - 0.77 μm) of GISS ModelE2.1 in Obiso et al. (2023).

Experiments		Emission (Tg/yr)	Load (Tg)	\overline{DAOD}	\overline{SSA}
HD27		3354	23.6	0.022	0.86
HD09		3119	21.5	0.020	0.93
VOL		3154	21.6	0.022	0.91
MG		3083	21.1	0.021	0.93
BM		3087	21.1	0.021	0.93
BM-RT	BM-LC	3097	21.1	0.021	0.930
	BM-LCRH	3069	20.9	0.021	0.930
	BM-LCRHRG	3110	21.4	0.021	0.928
AeroCom ⁽¹⁾		1600 (1000-3200)	20 (9-26)	0.029 (0.021 - 0.035)	-
CMIP5 ⁽²⁾		2700 (1700-3700)	17 (14-36)	-	-

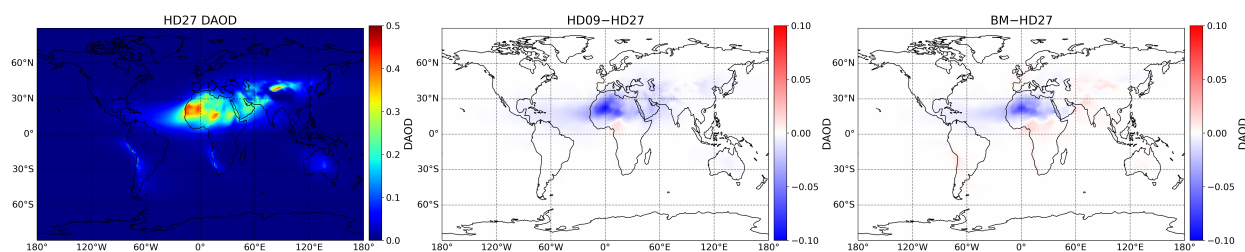
CMIP6 ⁽³⁾		3472	25	0.029	-
DUSTCOMM ⁽⁴⁾		4700 (3300 - 9000)	26 (22 - 31)	0.028 (0.024 - 0.030)	-
GISS ModelE2.1 ⁽⁵⁾	HOM	4031	31.3	0.020	0.917
	EXT	4152	32.4	0.020	0.936
	INT	4284	33.7	0.021	0.942
<p>(1) Results are from AeroCom Phase I, which were taken from Table 3 in Huneeus et al. (2011), and the 1 standard error range was obtained by eliminating the two highest and lowest values.</p> <p>(2) Results are from Table 3 in Wu et al. (2020)</p> <p>(3) Results from Zhao et al. (2022)</p> <p>(4) Results are from Table 3 in Kok et al. (2021)</p> <p>(5) Results from Obiso et al. (2023).</p>					

338

339 The lowest SSA of HD27 in Table 3 suggests that HD27 dust, which has been used in the standard
340 AM4.0 model, is the most absorptive among all experiments. The HD09 dust is much less
341 absorptive, attributed to its smaller hematite content, as indicated by the lower imaginary part of
342 RI in the visible range (Figure 1). For the three mineral-resolved experiments, the lower global
343 mean SSA (\overline{SSA}) in VOL suggests that VOL-mixing dust is more absorptive than MG-mixing
344 and BM-mixing dust. This finding is consistent with previous studies that have suggested that
345 VOL-mixing method, when applied to minerals to compute the bulk aerosol optical properties,
346 may artificially enhance absorption relative to scattering and lead to a lower SSA for bulk dust
347 aerosol (Zhang et al., 2015). We can see that the global mean SSA (\overline{SSA}) of HD09 dust is
348 comparable to the values obtained in cases where minerals are resolved (e.g., MG and BM). This
349 implies that, from a global perspective, HD09 dust is as absorptive as mineral-resolved dust (e.g.,
350 MG and BM).

351 In addition to the globally averaged dust properties listed in Table 3, we illustrate the distribution
352 of global dust mass across 5 size bins (Figure S3 in the Supplement) and the global distribution of
353 DAOD (Figure 2) for the three experiments: before (e.g., HM27 and HD09) and after (e.g., BM)
354 resolving mineralogy. The global dust mass distribution across the 5 size bins remains largely
355 unchanged across experiments. Besides the subtle difference (~10%) in global mean DAOD across

356 the three experiments as listed in Table 3, the global distribution of DAOD responds differently in
 357 HD09 and BM. Compared to HD27, reducing hematite content to HD09 generally decreases
 358 DAOD, except over the Sahel region. In contrast, resolving mineralogy as in BM decreases DAOD
 359 over the Sahara region while increasing DAOD over the Sahel and Asia regions. The reduction in
 360 DAOD over the Sahara region further contributes to the decrease in dust absorption over the region,
 361 primarily attributed to the change in dust optical properties, such as the enhancement in dust SSA.
 362 The indistinct variation in DAOD across different experiments results from the feedback of dust
 363 interactions with radiation (Miller et al., 2004; Pérez et al., 2006; Miller et al., 2014), which is
 364 influenced by the distinct scattering properties of dust aerosols in each experiment as shown in
 365 Table 3.

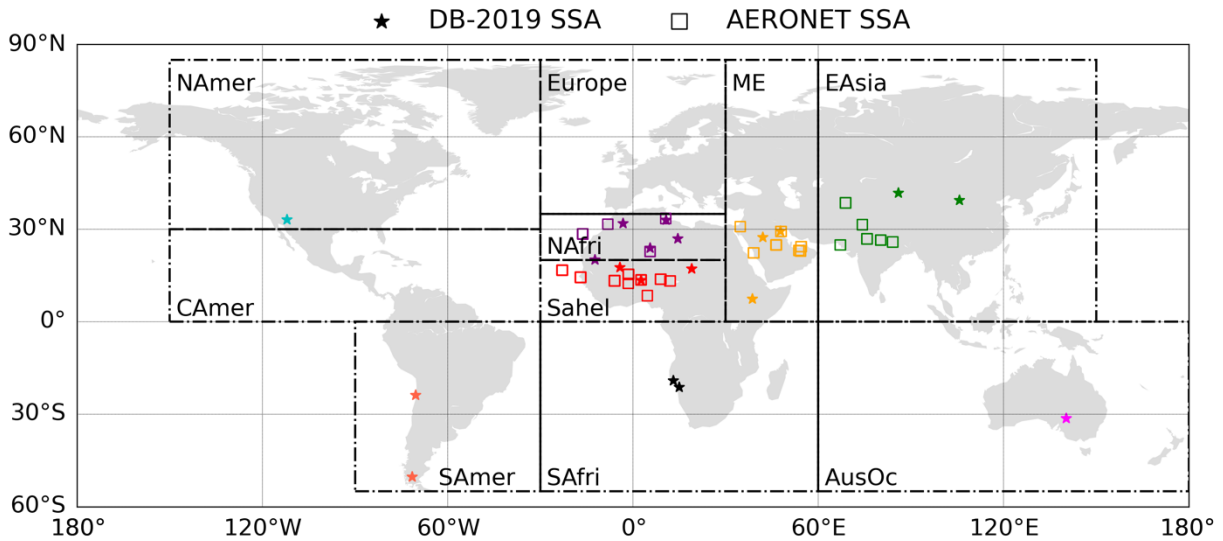


366
 367 Figure 2. The global distribution of dust optical depth (DAOD) for HD27, and the difference in DAOD
 368 between HD09 and BM compared to HD27. The global mean DAOD values (\overline{DAOD}) of each experiment
 369 are shown in Table 3.

370 4.2 Comparison of dust optical properties with observations

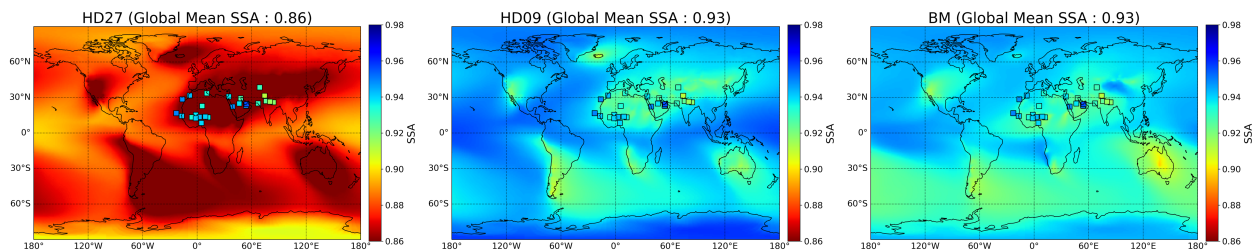
371 Iron oxides content of dust determines shortwave radiation absorption by dust: the higher amount
 372 of iron oxides, the lower the SSA. Following our calculations of dust optical properties in Section
 373 4.1, we compared GFDL AM4.0 modeled dust SSA (averaged in the visible band 0.44-0.625 μm)
 374 against AERONET SSA retrievals (averaged at two visible wavelength: 0.44 μm and 0.67 μm) in
 375 Section 4.2.1 and laboratory measurements of SSA (at 0.55 μm) in Section 4.2.2. The modeled
 376 dust SSA is evaluated against observation-based results utilizing the following evaluation metrics:
 377 the mean SSA (mSSA) is calculated based on SSA for all locations displayed in Figure 3, the
 378 standard deviation (σ), derived from SSA for all locations displayed in Figure 3, is used as an
 379 indicator of dust SSA spatial variation; the normalized mean bias (nMB) and normalized root
 380 mean square error ($nRMSE$) are utilized to assess the mean bias and root mean square error,
 381 respectively, of modeled SSA in comparison to observed SSA. Definitions of nMB and $nRMSE$
 382 are provided in Section S3 in the Supplement.

383 4.2.1 Comparison with AERONET retrievals

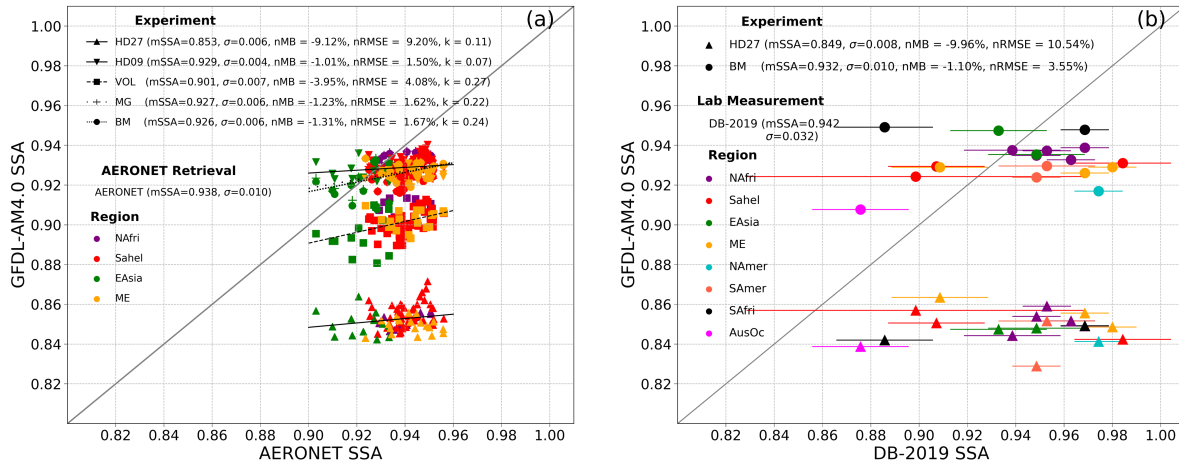


384
 385 Figure 3. Dust sample locations in Di Biagio et al. (2019) and AERONET stations selected by filtering dust
 386 events. AERONET stations for SSA retrievals are in North Africa (NAfri), Sahel, the Middle East (ME)
 387 and East Asia (EAsia). Lab measurements by Di Biagio et al. (2017, 2019) expand dust sampling to include
 388 soils from North America (NAmer), South America (SAmer), South Africa (SAfri), Australia (AusOc).

389 Figure 3 displays the AERONET stations selected by filtering dust events. The global distribution
 390 of modeled dust SSA and AERONET retrieved SSA over the selected AERONET sites are shown
 391 in Figure 4. There is a significant decrease in dust absorption from HD27 to HD09 globally due to
 392 the reduction in hematite content. HD09 and BM exhibit similar dust absorption on a global scale
 393 (e.g., the same global mean \overline{SSA}), but the regional differences are evident. For instance, compared
 394 to HD09, resolving mineralogy (e.g., BM) decreases dust absorption over Iceland and Taklamakan
 395 regions, while enhances dust absorption over Southern Hemisphere, particularly over Australia.
 396 Additionally, there is a shift in dust absorption from the Sahara to the Sahel region after resolving
 397 mineralogy.



398
 399 Figure 4. The 19-year (2001-2019) annual mean dust SSA simulated by AM4.0 across the three experiments.
 400 The squares represent 21-year (2000-2020) annual mean AERONET retrieved dust SSA over the selected
 401 AERONET sites.



402

403 Figure 5. GFDL AM4.0 modeled 19-year (2001-2019) averaged monthly dust SSA (average in 0.44-0.625
 404 μm) versus (a) AERONET 21-year (2000-2020) averaged monthly SSA retrievals (average at two visible
 405 wavelengths: 0.44 μm and 0.67 μm) and (b) laboratory SSA measurements (at 0.55 μm) of dust particles
 406 with diameter ranging from 0.2 μm up to 10 μm obtained by Di Biagio et al. (2019) (DB-2019). The lab
 407 measurements were carried out in March 2015, horizontal error bars represent measurement uncertainties.
 408 Markers represent different experiments, and colors represent different regions. mSSA in the legend
 409 represents the mean SSA averaged over all locations indicated in Figure 2 (squares for AERONET, stars
 410 for DB-2019). The standard deviation (σ), normalized mean bias (nMB), normalized root mean square error
 411 (nRMSE), and the slope of linear regression (k) are also indicated in the legend.

412 Figure 5a shows GFDL AM4.0 modeled 19-year (2001-2019) averaged dust SSA (average in 0.44-
 413 0.625 μm) versus AERONET SSA (average at 0.44 μm and 0.67 μm) retrievals. Compared to
 414 AERONET SSA retrievals, both HD27 and VOL overestimate dust absorption, as indicated by
 415 their relatively low SSA (Figure 5a). HD27 dust is the most absorptive, indicating that the standard
 416 AM4.0 dust is overly absorptive. Dust SSA in MG and BM are quite similar (i.e., mSSA: 0.926
 417 versus 0.927) and show a better agreement with AERONET measurements (nMB $\approx -1.3\%$ and
 418 nRMSE $\approx 1.6\%$), and they exhibit stronger scattering (i.e., higher SSA) than HD27 and VOL.
 419 HD09 is almost as scattering as MG and BM, as indicated by the mSSA of 0.929 versus 0.926 and
 420 0.927 in Figure 5a, which is consistent with the global mean SSA ($\overline{\text{SSA}}$) results shown in Table 3.
 421 Overall, both the fixed mineralogy dust HD09 and mineral-resolved MG and BM dust agree well
 422 with AERONET SSA retrievals, while HD27 and VOL are too absorptive. Therefore, we
 423 recommend using mixing ratios of MG or BM in calculating optical properties of internal mixture
 424 of hematite and clay minerals. Unless otherwise specified, in the following part of the paper, we
 425 will refer to mineral-resolved experiments as MG or BM.

426 We further assess the SSA spatial variation (indicated by σ) for each experiment from AM4.0 by
427 comparing it to observation-based results. SSA is generally determined by dust mineralogy, size
428 as well as shape. Various dust mineralogy leads to distinct dust SSA due to the different absorption
429 properties of minerals (Figure 1). Coarser dust generally tends to be more absorptive (i.e., has
430 lower SSA) than finer dust when other factors are the same (Ryder et al., 2018). Spherical dust
431 assumption tends to underestimate dust SSA (Huang et al., 2023). Given the uncertainty in dust
432 shape, we assume dust particles to be spherical in this study, aligning with other model studies
433 (e.g. Glib et al., 2021). Consequently, in the mineral-resolved experiments of this study, namely
434 VOL, MG, and BM, dust mineralogy and dust size are the two factors affecting the SSA spatial
435 variation.

436 Conversely, in homogeneous dust experiments, specifically HD27 and HD09, SSA variation is
437 solely attributed to variation in dust size, as dust mineralogy remains uniform globally.
438 Interestingly, HD09 demonstrates smaller spatial variation (i.e., lower σ) in SSA compared to
439 HD27 (Figure 5a). To investigate the impact of dust size on SSA for different hematite content
440 (e.g., HD27 and HD09), we perform a simple test in Section S4 of the Supplement. Supplementary
441 Figure S4 and S5 illustrate that the variation of SSA due to the dust particle size is more
442 pronounced with increasing absorption, i.e., from HD09 to HD27. This suggests that enhancement
443 in dust scattering relative to dust absorption (i.e., an increase in SSA) mitigates the sensitivity of
444 SSA to dust size.

445 The conclusions above provide an understanding of the SSA spatial variation (indicated by σ)
446 before (i.e., HD27 and HD09) and after (i.e., VOL, MG, and BM) implementing dust mineralogy.
447 The same σ (0.06) between HD27 and BM can be explained as follows: Because mineral-resolved
448 BM-mixing dust is overall more scattering than HD27 dust, resulting in a reduced sensitivity of
449 SSA to size, therefore, the σ of SSA caused by dust size is reduced in BM relative to HD27.
450 However, the incorporation of dust mineralogy in BM leads to an increase of σ . These contrasting
451 effects compensate for each other, resulting in the same σ . In contrast, HD09 is overall as
452 scattering as BM, as shown in Table 3 and Figure 5a, suggesting a similar sensitivity of SSA to
453 size. Therefore, the incorporation of dust mineralogy in BM results in a higher σ compared to
454 HD09. Overall, while the enhancement in σ can be offset by the reduction in σ due to the reduced

455 sensitivity to dust size, resolving dust mineralogy increases σ on its own, consequently enhancing
456 the spatial variation in dust SSA.

457 Worth to mention, AERONET dust is quite scattering as shown in Figure 5a, therefore its SSA is
458 less sensitive to dust size. The high σ (0.010) of AERONET SSA can be mainly due to spatial
459 variations in dust mineral composition. Reducing dust hematite content (HD09) leads to a better
460 agreement in mean SSA with AERONET (i.e., more scattering dust) but results in very low σ
461 (0.004), while implementing dust mineralogy (e.g., MG and BM) retains the agreement with
462 AERONET in mean SSA and, at the same time, increases σ (0.006).

463 Besides the standard deviation (σ), the slopes (k) obtained from the statistics of modeled SSA
464 versus AERONET SSA can also indicate the regional contrast of SSA. The regional contrast of
465 AERONET SSA is well captured by the model when k is one, underestimated when k is lower than
466 one, and overestimated when k is higher than one. As such, the slopes in Figure 5a show that the
467 contrast in SSA from different regions (e.g., North Africa vs. East Asia) observed by AERONET
468 is better captured by mineral-resolved experiments (e.g., VOL, MG and BM with k ranging from
469 0.22 to 0.27) than homogeneous dust experiments (e.g., HD27 and HD09 with k ranging from 0.07
470 to 0.11). However, the modeled regional contrast of SSA in mineral-resolved experiments remains
471 overly underestimated (i.e., k is much lower than one). The significant underestimation of regional
472 SSA contrast (k) and spatial variation (σ) in AM4.0, even after accounting for mineralogy, implies
473 that something important is still missing in models. For instance: 1) the observed regional contrast
474 in iron oxides content may be higher than that in the soil map used in this study, and 2) the model
475 may have underestimated regional contrasts in the dust aerosol size distribution and thus their
476 contribution to SSA, and 3) spatial variation of dust shape, which is not taken into account in the
477 model.

478 4.2.2 Comparison with laboratory measurements

479 We further compare the GFDL AM4.0 modeled dust SSA (average in 0.44-0.625 μm) with DB-
480 2019 laboratory measurements of SSA at 0.55 μm (Figure 5b). Figure 3 shows the locations where
481 dust samples were collected for the lab measurements. Considering that MG and BM are very
482 similar in terms of dust absorption and agree the best with AERONET SSA, we select BM as a
483 representative to compare with DB-2019 SSA. Moreover, to evaluate how dust absorption is
484 represented in the standard AM4.0 relative to lab measurements, we also show the comparison of

485 SSA between HD27 used in the standard AM4.0 and DB-2019 (Figure 5b). Consistent with the
486 comparison with AERONET, the comparison with lab measurements suggests that dust
487 representation in the standard AM4.0 (i.e., HD27) is excessively absorptive. The smaller nMB and
488 nRMSE values in BM suggests that SSA of BM agrees better with lab measurements.

489 Moreover, regarding spatial variation (σ), resolving dust mineralogy in BM increases σ from 0.008
490 for HD27 to 0.010 for BM, even though it is still lower than the σ (0.032) in DB-2019 lab
491 measurements. Note that the variation for HD27 results from the high sensitivity of SSA to dust
492 size due to its higher absorption (as discussed in Supplementary Section S4). The inability to
493 reproduce spatial variation observed in the lab measurements is likely attributed to two aspects.
494 The first limitation is the fact that samples of DB-2019 are from soils rather than aeolian dust.
495 Aeolian dust is expected to exhibit greater uniformity in mineralogy than soils because of the
496 atmospheric mixing of dust emitted from various soil sources. The second one is associated with
497 the under-representation of regional contrast in iron oxides content in our model. Observations
498 from the EMIT are therefore essential to constrain soil mineralogy in climate models.

499 **5 Impacts of dust mineralogy on climate**

500 Resolving dust mineralogy in climate models affects dust optical properties (as discussed in
501 Section 4) and their spatial and temporal variability, thereby affecting their interactions with
502 shortwave (SW) and longwave (LW) radiation. The variability in dust radiative interactions further
503 induces the fast response of land surface temperature, circulation, and precipitation. To investigate
504 the impacts of resolving dust mineralogy on climate, we need to compare modeled results in
505 mineral-resolved experiments to the baseline homogeneous dust (i.e., non-resolved mineralogy)
506 control run. As a result, the significance of the impacts depends on the selection of the baseline
507 homogeneous dust experiment. In this section, we investigate the impacts of resolving dust
508 mineralogy compared to two baseline homogeneous dust experiments. One baseline experiment is
509 the homogeneous dust used in the standard GFDL AM4.0, in which dust mineralogy is assumed
510 to be temporally and spatially uniform (i.e., non-resolved), with a volume fraction of 2.7%
511 hematite (HD27). The impacts of resolving dust mineralogy, compared to the baseline HD27, can
512 be attributed to two factors: 1) the reduction in dust absorption after resolving dust mineralogy in
513 comparison to HD27 as discussed in Section 4, and 2) spatial and temporal variations in dust
514 scattering properties induced by inhomogeneity in dust mineralogy. The other baseline experiment

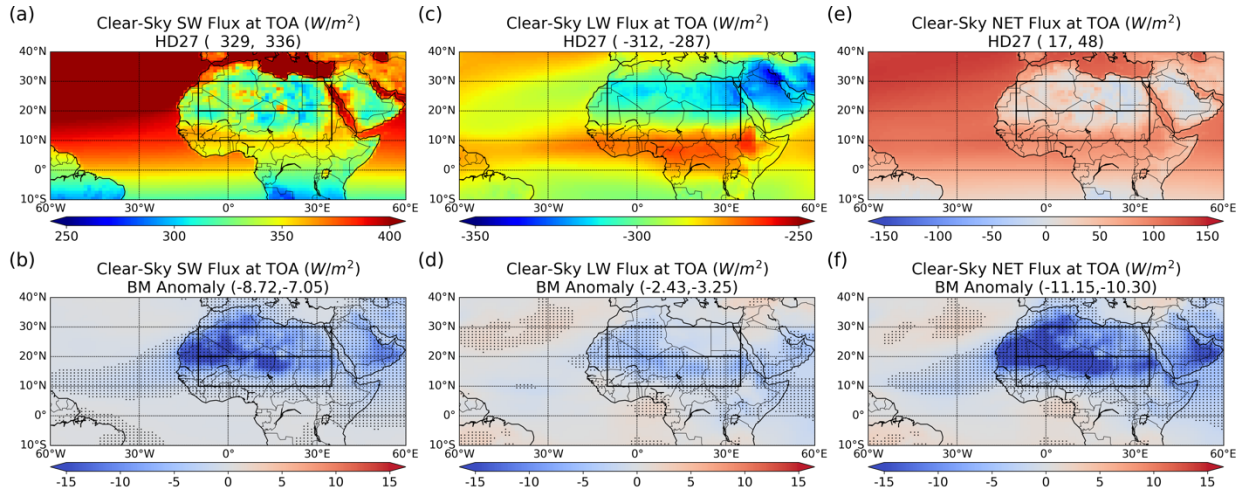
515 is the homogeneous dust, with a volume fraction of 0.9% hematite (HD09). Given the comparable
516 global mean dust scattering properties (e.g., \overline{SSA}) between the control run HD09 and mineral-
517 resolved experiments (e.g., MG and BM), the impacts of resolving dust mineralogy, compared to
518 baseline HD09, is solely attributed to the inhomogeneity in dust scattering properties induced by
519 resolving dust mineralogy.

520 **5.1 Impacts on Clear-sky Radiative Fluxes**

521 We start our analysis by examining the impacts of resolving dust mineralogy on clear-sky radiative
522 fluxes. By ‘clear-sky’, we mean that our results do not consider the radiative effects of clouds. We
523 use anomalies (ΔF) to evaluate the impacts of resolving mineralogy on clear-sky radiative fluxes,
524 which is defined as, $\Delta F = F_1^\uparrow - F_2^\uparrow$, where F_1^\uparrow is the 19-year mean clear-sky upward radiative
525 fluxes with resolved mineralogy, F_2^\uparrow is the 19-year mean clear-sky upward radiative fluxes for
526 homogeneous dust. Section S5 in the Supplement provides the clear-sky radiative fluxes anomalies
527 at TOA and surface (SFC) induced by resolving dust mineralogy over the global scale, we see
528 much more significant anomalies over the North Africa than other regions, which makes sense
529 because that dust aerosol is the most dominant aerosol species in this area. The changes in dust
530 aerosol optical properties have a greater potential to lead to significant impacts on radiation and
531 climate over the region than in the others. Therefore, this section focuses on the North Africa
532 region, where the Sahara Desert, the largest dust source in the world, is located. The Sahara (20°N-
533 30°N, 10°W-35°E) and the Sahel (10°N-20°N, 10°W-35°E) regions are studied separately. We
534 specifically analyze the results for the June-July-August (JJA) season when dust loading is at its
535 highest and the West African Monsoon is the strongest.

536 **5.1.1 Impacts on Clear-sky Radiative Fluxes relative to HD27**

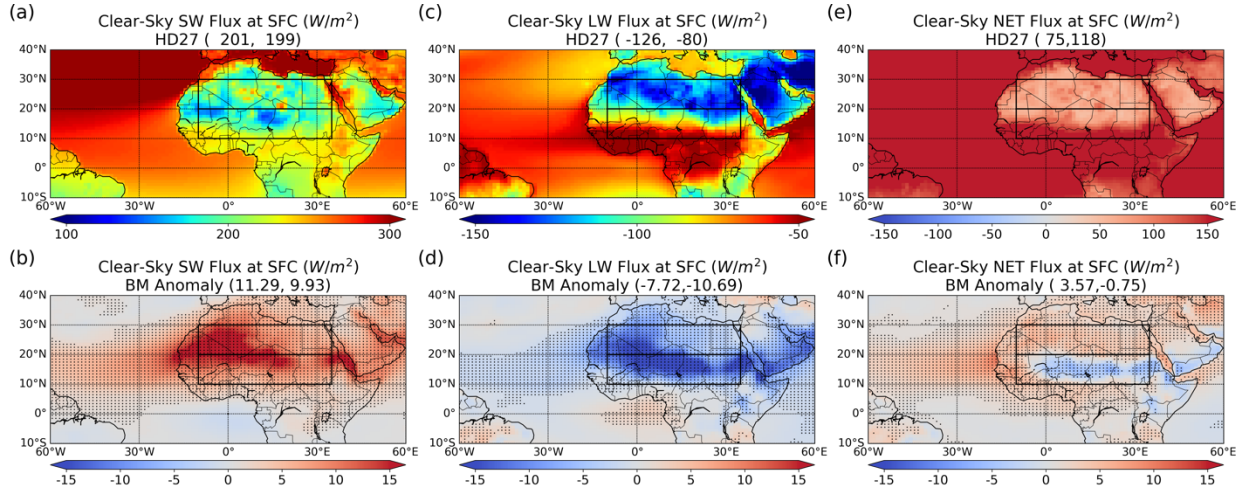
537 Before comparing mineral-resolved experiments (e.g., BM) with HD27 control run, the dust has
538 been used in the standard GFDL AM4.0, to understand their impacts on clear-sky radiative fluxes
539 relative to HD27, it’s worth recapping that the effects of resolving mineralogy relative to HD27
540 can be attributed to two factors: the reduction in dust absorption and the variation in dust scattering
541 properties induced by the mineralogical inhomogeneity.



542

543 Figure 6. Seasonal mean JJA climatology (2001-2019) clear-sky SW (1st column), LW (2nd column) and
 544 Net (3rd column) radiative flux at TOA for the HD27 control run (1st row) and their anomalies resulting
 545 from resolving dust mineralogy in Bruggeman-mixing experiment (2nd row). Downward direction is defined
 546 as positive. The dotted area denotes anomalies that are statistically significant. The two values in
 547 parentheses within the title of each figure are domain average for the Sahara and Sahel regions.

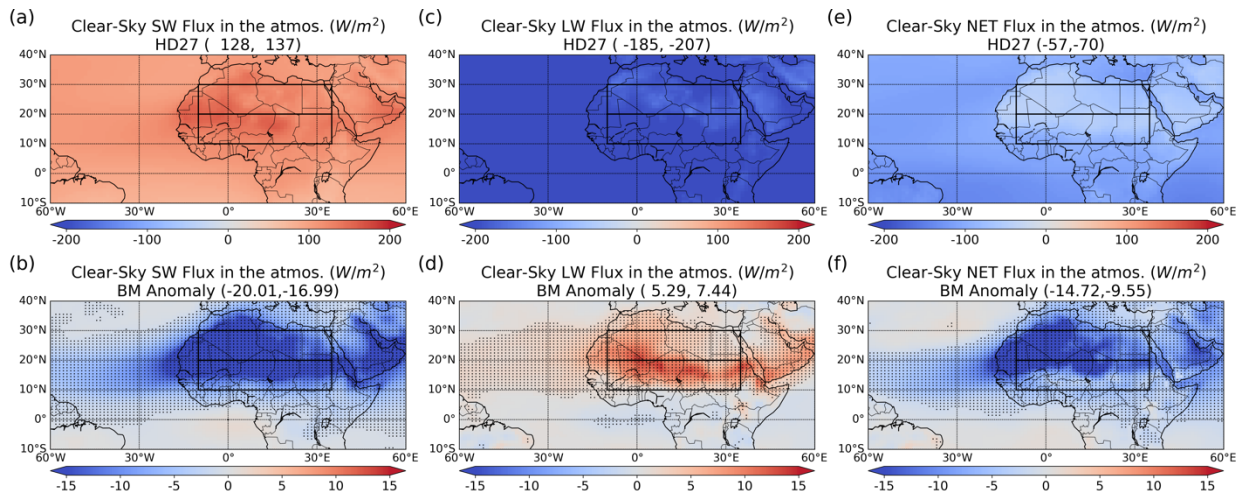
548 The first row in Figure 6 illustrates the modeled clear-sky shortwave (SW), longwave (LW) and
 549 net (NET: the combination of SW and LW) radiative flux at TOA from the HD27 control run.
 550 Relative to HD27, mineral-resolved dust (e.g., BM-mixing dust) generally reflects more SW
 551 radiation back to space and induces negative SW flux anomalies at TOA (Figure 6a, b; Positive:
 552 downward). Relative to the HD27 control run, the LW flux anomaly at TOA resulting from
 553 resolving mineralogy is less substantial compared to SW flux anomaly (Figure 6c, d). After
 554 combining both SW and LW, resolving mineralogy turns out to induce substantial decrease in NET
 555 flux at TOA, with a more than 50% negative anomaly over the Sahara and around a 20% negative
 556 anomaly over the Sahel (see values in parentheses in Figure 6e, f). Therefore, less NET radiation
 557 reaches the Earth at TOA in the mineral-resolved dust cases due to their lower absorptivity.



558

559 Figure 7. As in Figure 6, but for the surface.

560 At the surface (SFC) in Figure 7, the enhanced scattering of mineral-resolved dust scatters more
 561 SW radiation toward Earth's surface, leading to a positive SW flux anomaly at SFC (Positive:
 562 downward). In the LW, the cooling of the mineral-resolved dust layer, due to its low absorption,
 563 results in less LW radiation being emitted toward Earth's surface. This reduction in the downward
 564 LW emission outweighs the change in the upward LW emission from the Earth's surface, thereby
 565 causing a negative LW flux anomaly at SFC. The positive anomalies in SW radiation are
 566 approximately canceled out by the negative anomalies in LW radiation (Figure 7). As a result, a
 567 similar amount of radiation reaches the Earth's surface in both HD27 and mineral-resolved cases.
 568 Despite less NET radiation entering the Earth at TOA in mineral-resolved cases, the similar
 569 amount of NET radiation reaching the Earth's surface indicates that less NET radiation is absorbed
 570 in the atmosphere in mineral-resolved cases.



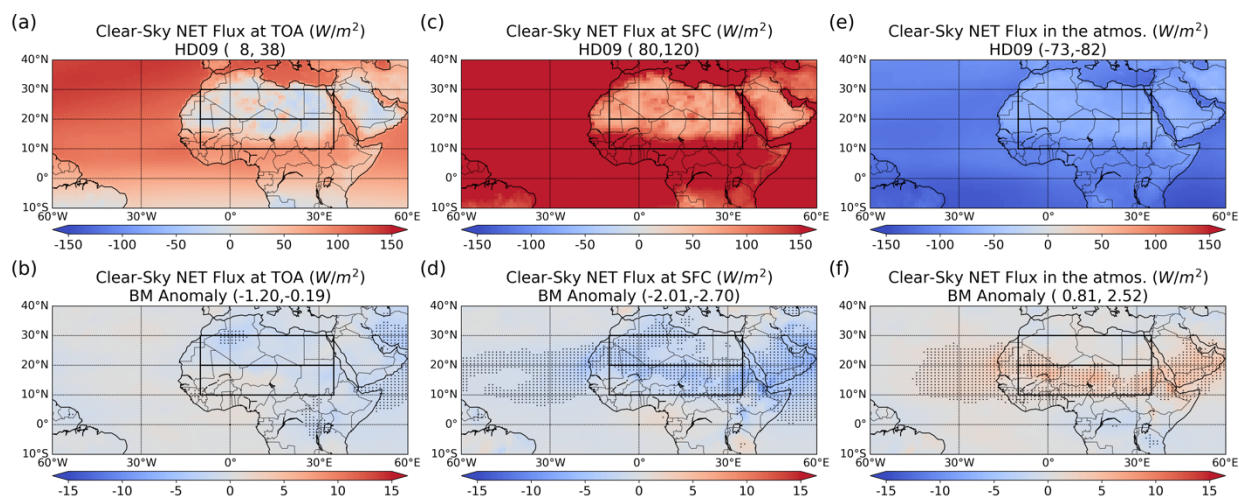
571

572 Figure 8. As in the Figure 6, but for the radiative flux absorbed in the atmosphere.

573 In Figure 8, the negative SW flux anomalies are partially offset by positive LW flux anomalies,
574 resulting in negative NET flux anomalies in the atmosphere. These anomalies amount to
575 approximately a 25% reduction over the Sahara and 10% reduction over the Sahel (see values in
576 parentheses in Figure 8b, d, f).

577 5.1.2 Impacts on Clear-sky Radiative Fluxes relative to HD09

578 Before comparing mineral-resolved experiments with HD09 control run, where the homogeneous
579 dust is as absorptive as mineral-resolved dust (e.g., MG and BM) from a global perspective, to
580 understand their impacts on clear-sky radiative fluxes relative to HD09, it's worth recapping that
581 the effects of resolving mineralogy relative to HD09 are primarily attributed to the variation in
582 dust scattering properties induced by the mineralogical inhomogeneity.



583
584 Figure 9. As in the Figure 6, but for HD09 control run. In addition, SW and LW flux anomalies are not
585 shown here. Clear-sky net flux at TOA (1st column), at surface (2nd column), and in the atmosphere (3rd
586 column) are shown in this figure.

587 **Error! Reference source not found.** Figure 9 shows the clear-sky fluxes anomalies with respect to
588 HD09 over North Africa, the anomalies over the global scale are shown in Figure S7, S9, S11
589 and S13 in the Supplement.

590 In contrast to the anomalies with respect to HD27 control run, resolving dust mineralogy does not
591 cause substantial anomalies (< 5%) in clear-sky fluxes with respect to HD09 control run. This can
592 be attributed to their similarity in dust scattering properties from a global mean perspective,
593 particularly SSA as shown in Figure 5. The comparable effects of HD09 and mineral-resolved dust

594 on radiation suggest that resolving dust mineralogy does not have significant impacts on clear-sky
595 fluxes when homogeneous dust is as scattering as mineral-resolved dust aerosols on a global scale.
596 However, the equivalence between HD09 and mineral-resolved dust in terms of their interactions
597 with radiation may be related to the three limitations in the current model simulations: 1) Soil
598 mineralogy: The limited soil mineralogy database fails to adequately capture the regional variation
599 of iron content (or SSA) within the region; 2) Dust emission based on Ginoux et al. (2001) uses a
600 continuous function of topography, which does not take into account geomorphological
601 characteristics of the surface to differentiate soil properties of dust sources as done by others
602 (Zender et al., 2003; Bullard et al., 2011); 3) Dust transport: Excessive numerical diffusion may
603 occur when solving advection equation (Ginoux, 2003). Given all those limitations of our model
604 simulations, this finding may differ with improved representation of dust sources and transport.
605 Such improvement may come from spaceborne soil mineralogy dataset (e.g., EMIT) that may
606 capture accurately the regional contrasts in iron oxides content.

607 5.1.3 Compare Clear-sky Radiative Fluxes with CERES Observations

608 Furthermore, we conduct a comparison of modeled SW upward, LW upward, NET downward flux
609 at TOA with observation-based results from CERES_EBAF_Ed4.2 product (see Table 4). The
610 difference between modeled flux and CERES observations are listed in parentheses within the title
611 of each figure in Table 4. Compared to HD27, the more scattering HD09 and mineral-resolved BM
612 achieve much better agreement with CERES observations in clear-sky flux (i.e., SWup, LWup and
613 NETdn) at TOA. This is evident in the smaller values of HD09 – CERES (e.g., NETdn: 1.6 for the
614 Sahara and 2.4 for the Sahel) and BM – CERES (e.g., NETdn: 0.4 for the Sahara and 2.1 for the
615 Sahel) compared to HD07 – CERES (e.g., NETdn: 11.3 for the Sahara and 12.4 for the Sahel), as
616 shown by the values in parentheses in Table 4. Between HD09 and BM, BM tends to agree slightly
617 better with CERES.

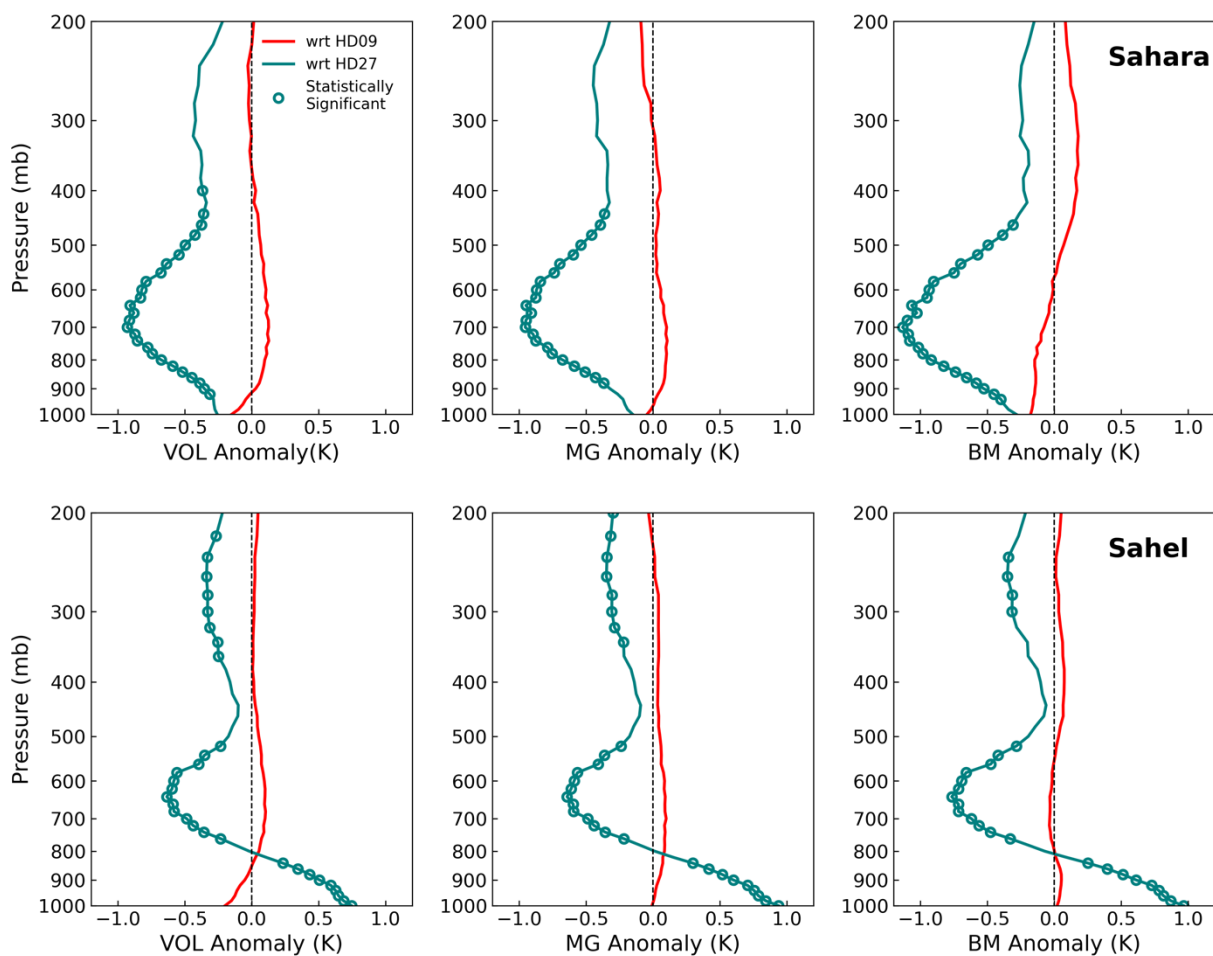
618 Table 4. Comparison of modeled clear-sky SW upward (SWup, 1st row), LW upward (LWup, 2nd row) and
619 NET downward (NETdn, 3rd row) fluxes at TOA with CERES observation-based results over 2001-2019
620 JJA. The 1st column shows the clear-sky flux estimates at TOA from CERES_EBAF_Ed4.2 product, which
621 represents clear-sky flux with clouds removed from the atmospheric column. The following columns show
622 the difference of modeled clear-sky flux at TOA in HD27 (2nd column), HD09 (3rd column) and BM (4th
623 column) experiments from CERES observations. The two values in parentheses represent domain average
624 for the Sahara and Sahel regions as indicated in figures in Section 5.1.2. Specifically, the first column
625 (CERES) is domain averaged flux, while the second (HD27 – CERES), third (HD09 – CERES), and fourth
626 (BM – CERES) columns are domain averaged flux differences between model and CERES observation-
627 based results.

	CERES	HD27 – CERES	HD09 – CERES	BM – CERES
Clr SWup flux at TOA (W/m ²)	(135, 113)	(-9.3, -9.4)	(-1.1, -2.2)	(-0.6, -2.3)
Clr LWup flux at TOA (W/m ²)	(314, 291)	(-1.4, -3.1)	(-0.6, -0.5)	(0.2, -0.1)
Clr NETdn flux at TOA (W/m ²)	(6, 36)	(11.3, 12.4)	(1.6, 2.4)	(0.4, 2.1)

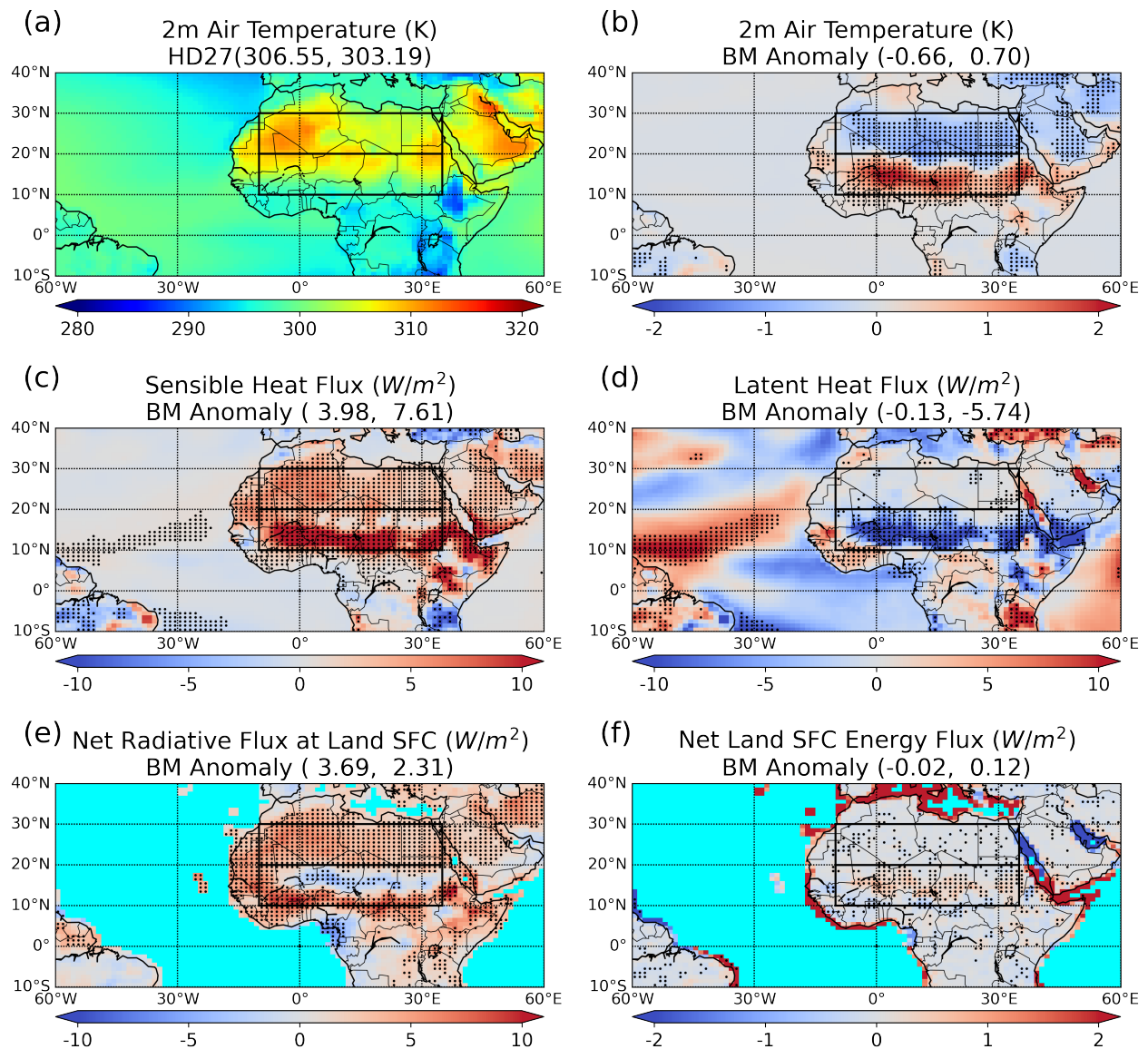
628

629 **5.2 Impacts on land temperature**

630 Here we explore the impacts on the temperature vertical profile and near-land surface temperature
631 relative to HD27 and HD09, respectively. Compared to the HD27 control run, lower absorption of
632 radiation in the atmosphere by mineral-resolved dust aerosols results in statistically significant
633 negative temperature anomalies in the atmosphere ranging from 800 mb up to 500 mb where dust
634 aerosols are mainly located (Figure 10). In contrast, there is no statistically significant temperature
635 anomaly for mineral-resolved dust cases compared to HD09, as illustrated by the red curves in
636 Figure 10 This finding aligns with the insubstantial anomalies (<5%) in clear-sky NET radiative
637 fluxes discussed in Section 5.1.2. In the subsequent part of the section, we will delve into
638 comparing mineral-resolved experiment (using BM as an example) with the HD27 control run.
639 This comparison will help us further understand the impact of dust aerosols with distinct
640 absorption on land temperature.



641
 642 Figure 10. Vertical profile of temperature anomaly induced by resolving dust mineralogy for the Sahara (1st
 643 row) and the Sahel (2nd row) regions in the three mineral-resolved experiments (i.e., VOL, MG, BM). Green
 644 lines represent temperature anomalies with respect to HD27 control run. Red lines are temperature
 645 anomalies with respect to HD09 control run. The circles represent statistically significant temperature
 646 anomaly.



647

648 Figure 11. Air temperature at 2-meter from HD27 control run (a), anomaly (b) induced by implementing
 649 Bruggeman-mixing minerals in BM experiment, surface sensible heat flux (c), latent heat flux (d), net
 650 radiative flux (e), net energy flux (f) anomalies between BM and HD27; Upward flux is positive in (c) and
 651 (d), while downward flux is positive in (e) and (f). Net energy flux (f) is the subtraction of (c), (d), and
 652 downward ground flux from (e). Note that ground flux is not shown in the figure considering its relatively
 653 small magnitude, but it is included in the land surface net energy flux calculations in subplot (f). The dotted
 654 area denotes anomalies that are statistically significant. The two values in parentheses within the title of
 655 each figure are domain average for the Sahara and Sahel regions.

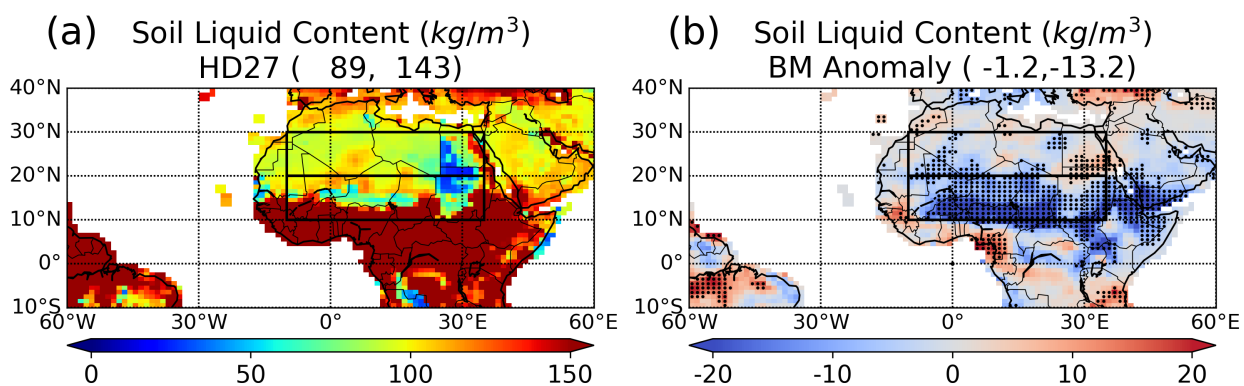
656 Figure 11a shows air temperature at 2-meter from HD27 control run over the Northern Africa.

657 Near the land surface, more scattering mineral-resolved dust induces a temperature decrease (i.e.,

658 negative temperature anomaly -0.66 K) over the Sahara and a temperature increase (i.e., positive

659 temperature anomaly 0.70 K) over the Sahel as shown Figure 11b. To understand this phenomenon,
660 we further analyze the surface energy budget in Figure 11c-f.

661 Radiative flux perturbation over land is quickly equivalented by balancing surface radiative fluxes
662 with sensible heat flux, latent heat flux and ground flux (i.e., downward heat flux into the ground),
663 which results in nearly zero net energy flux at land surface as shown in Figure 11f. Precisely, the
664 radiative flux anomaly comprises two contributions: one is the instantaneous radiative forcing (IRF)
665 caused by the change in dust mineralogy in the atmosphere, and the other one is the associated
666 radiative feedbacks. For simplicity, we will not partition the radiative flux anomaly in our
667 discussion here. Over the Sahel region, the positive net radiative flux anomaly at land surface is
668 balanced out by the increased sensible heat flux and the decreased latent heat flux as well as ground
669 flux. Note that the ground flux is generally small in magnitude and not shown in Figure 11, but we
670 include it in calculating net surface energy flux in Figure 11f. The decrease of latent heat flux over
671 the Sahel in BM case (Figure 11d) is due to the depletion of soil moisture (and therefore
672 evaporation) in the region as shown in Figure 12. The depletion of soil moisture is caused by the
673 decrease in moisture carried by onshore winds over the Sahel and the decrease in precipitation
674 over the same region, as will be discussed in section 5.3. Therefore, a large enhancement of
675 sensible heat flux ($\sim 7.6 W/m^2$) is needed (Figure 11c) not only to compensate for the depletion
676 in latent heat flux ($\sim 5.7 W/m^2$ in d), but also to balance out the increased net radiative flux (~ 2.3
677 W/m^2 in Figure 11e). As a result, higher land surface temperature with anomaly around 0.7 K is
678 needed in the region to achieve the required sensible heat flux enhancement.



679
680 Figure 12. Soil liquid content in HD27 control run (a) and anomaly resulting from implementing
681 Bruggeman-mixing minerals in the BM experiment (b). The two values in parentheses within the title of
682 each figure are domain average for the Sahara and Sahel regions.

683 Over the Sahara region, latent heat flux does not change from HD27 case to BM case, therefore,
 684 the increased net radiative flux ($\sim 3.69 \text{ W/m}^2$) in BM compared to HD27 is mainly balanced out
 685 by the enhanced sensible heat flux ($\sim 3.98 \text{ W/m}^2$) which requires a larger temperature gradient
 686 between surface and atmosphere. However, there is a very strong negative temperature anomaly
 687 (around -1K) in the atmosphere near 700 hPa due to less dust absorption in BM as we discussed
 688 in Figure 10. The strong negative temperature anomaly in the lower atmosphere effectively
 689 increases the vertical temperature gradient. As such, it is not necessary for the land surface
 690 temperature to increase; in fact, it may need to decrease by approximately 0.66 K to achieve the
 691 desired enhancement in sensible heat flux and reach equilibrium.

692 Additionally, to assess the effectiveness of various dust scattering properties (e.g., HD27, HD09,
 693 and BM) in matching observations of near-surface temperature, we compare the modeled near
 694 surface temperature (T_{2m}) with CRU TS observations, which is described in Section 2.6, over the
 695 Sahara and Sahel regions (Table 5). Considering the relatively large inter-model spread of regional
 696 surface air temperature, we compare the Sahara-Sahel regional contrast in surface air temperature
 697 to the CRU rather than comparing their absolute values. Table 5 shows that HD09 and BM improve
 698 the agreement with CRU in Sahara-Sahel temperature contrast compared to HD27, and BM
 699 exhibits the closest agreement with CRU.

700 **Table 5.** The 19-year (2001~2019) JJA mean 2-meter Air Temperature (T_{2m} , unit: K) and their standard
 701 deviation over the 19 years from CRU observations and modeled experiments over the Sahara and Sahel
 702 regions. The ‘Contrast’ row indicates the T_{2m} regional contrast between the Sahara and the Sahel.

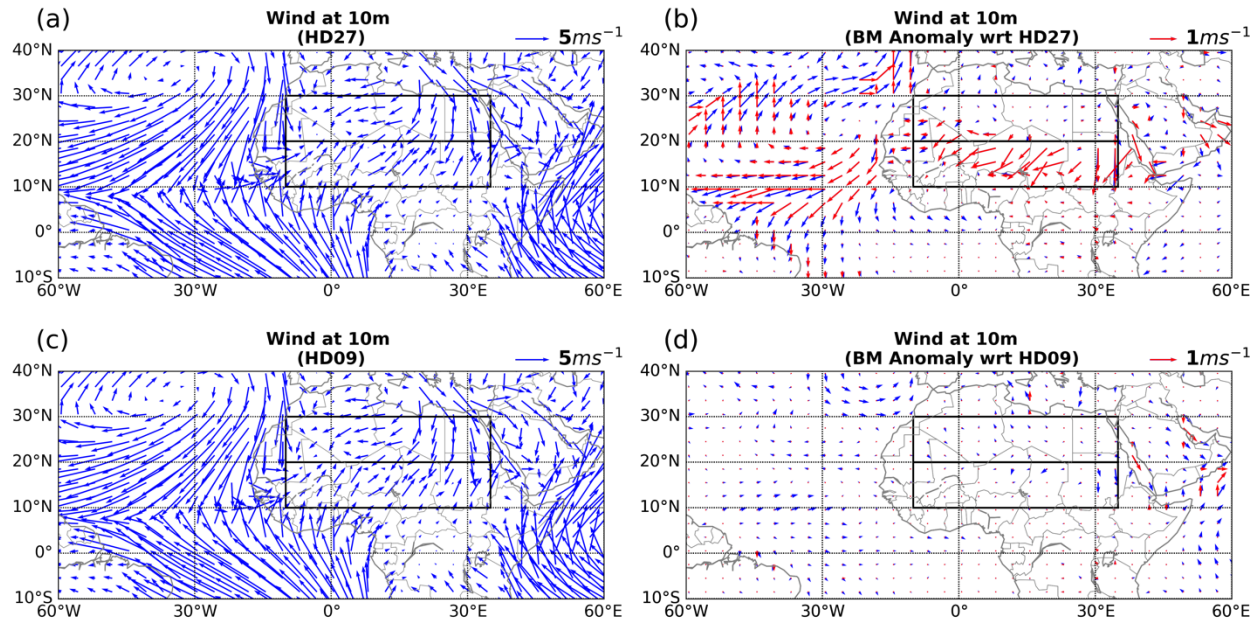
Region	CRU (K)	HD27 (K)	HD09 (K)	BM (K)
Sahara	305.8 ± 0.18	306.55 ± 0.52	306.2 ± 0.68	305.89 ± 0.61
Sahel	304.1 ± 0.32	303.19 ± 0.46	303.87 ± 0.51	303.89 ± 0.59
Contrast	1.7 ± 0.5	3.36 ± 0.98	2.3 ± 1.19	2.0 ± 1.2

703

704 **5.3 Impacts on winds and precipitation**

705 To understand the fast circulation and hydrological response resulting from resolving dust
 706 mineralogy, we examine surface wind speed anomalies (Figure 13) and precipitation anomalies

707 (Figure 14) induced by mineral-resolved dust. We compare mineral-resolved experiments (using
 708 BM as an example) with HD27 and HD09, respectively, to investigate the effects of resolving dust
 709 mineralogy.



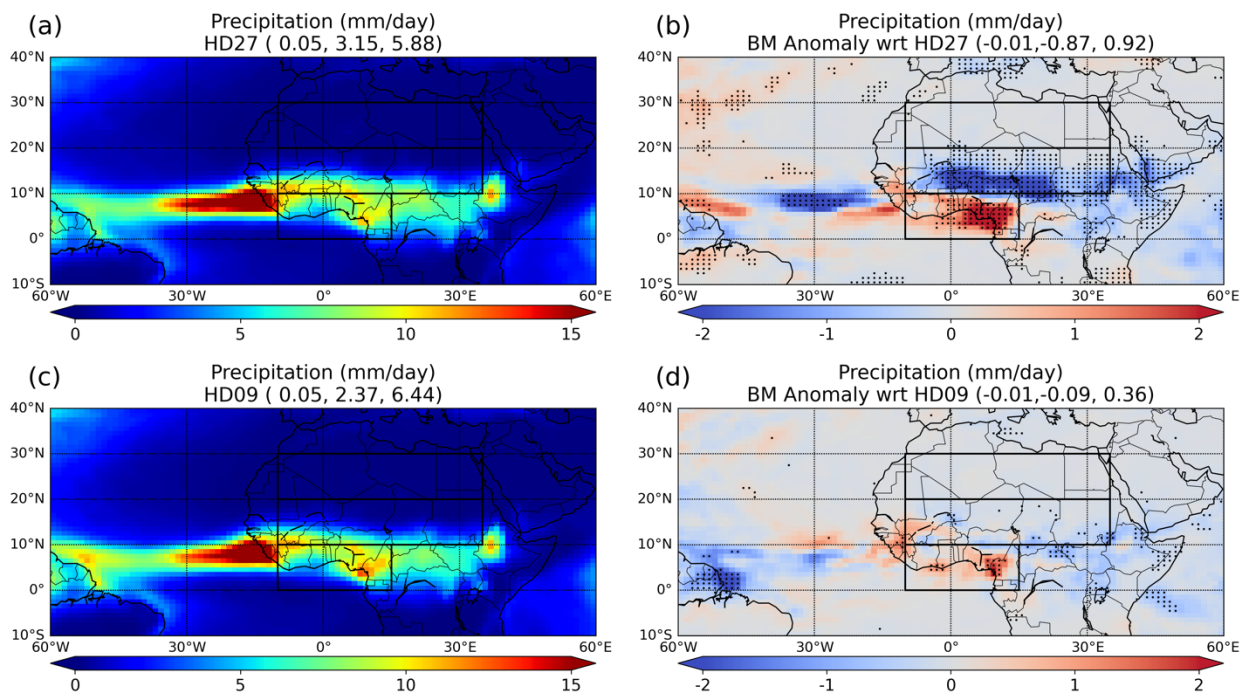
710
 711 Figure 13. Surface wind at 10-meter from HD27 (a) and HD09 (c) control runs and their anomalies (b) and
 712 (d) resulting from implementing Bruggeman-mixing minerals in the BM experiment. Statistically
 713 significant wind anomalies are highlighted by red arrows.

714 Global precipitation is higher by 0.017 mm/day for the BM mineral-speciated case compared to
 715 HD27 experiment. This is consistent with the lower SW absorption in the former, given the global
 716 compensation between latent heating associated with precipitation and net radiative cooling (e.g.,
 717 Allen and Ingram, 2002; Samset, 2022). (Global radiative cooling is also compensated, although to a
 718 smaller extent, by the sensible heat flux.)

719 However, within the Sahel, precipitation for BM is reduced compared to HD27 (Figure 14b), with
 720 weaker onshore flow during the summer monsoon (Figure 13b), displacing West African
 721 precipitation toward the Guinea coast. This reduction is consistent with several previous
 722 calculations of the fast response calculated with fixed SST (e.g., Stephens et al., 2004; Miller et
 723 al., 2004b; Lau et al., 2009; Jin et al., 2016; Jordan et al., 2018).

724 Dust absorbs radiation and redistributes heating from the surface to within the dust layer (Miller
 725 and Tegen, 1999; Strong et al., 2015). The heating of the air warms the lower to middle troposphere,
 726 thereby enhancing upward motion. The rising warm air spawns a large-scale onshore flow,

727 carrying the low-level moist air from the Atlantic to the Sahel, thus enhancing precipitation over
 728 this region (Balkanski et al., 2021). The more scattering mineral-resolved BM and MG dust absorb
 729 less radiation and cause less warming of the atmosphere (Section 4.1), reducing adiabatic cooling
 730 through ascent and Sahel precipitation. The suppressed ascent in BM compared to HD27 is
 731 associated with a reduction both in the wind divergence aloft and in convergence at the surface
 732 (Figure 13b). The reduction in convergence results in northeast wind anomalies at 10-meter over
 733 the Sahel (Figure 13b), which are opposite in direction to the southwest onshore winds of the West
 734 African Monsoon (Figure 13a). The inhibition of onshore winds, bringing less moisture to the
 735 Sahel, is consistent with the reduction of ascent and precipitation over this region (Figure 14a, b).



736
 737 Figure 14. 19-year (2001-2019) JJA mean precipitation from HD27 (a) and HD09 (c) control runs and
 738 anomalies resulting from implementing Bruggeman-mixing minerals with respect to HD27 (b) and with
 739 respect to HD09 (d). The three values in the parenthesis are domain averaged values for the Sahara, Sahel,
 740 and GC regions.

741 Besides the Sahel, there is a statistically significant positive anomaly (0.92 mm/day) of
 742 precipitation over the region to the south of the Sahel in BM relative to HD27 (Figure 14b). We
 743 will call this region the Guinea Coast (GC: 0-10°N, 10°W-15°E) region. One possible reason for
 744 the increase of precipitation over the GC is that the region is located to the south of the Saharan
 745 dust layer, where the suppression of ascent over the Sahel in BM suppresses the subsidence in the
 746 GC region and, therefore, enhances the precipitation (Guo et al. 2021). Alternatively, the moist

747 onshore flow that is weakened in BM is subject to greater dilution by the dry desert air, resulting
748 in reduced moist static energy and buoyancy, limiting convection to the coastal region.

749 These changes in precipitation have non-negligible effects on soil moisture content in North Africa
750 due to its moisture-starved environment. The decrease in precipitation over the Sahel in BM leads
751 to a reduction in soil moisture content. Conversely, the increase of precipitation over the GC leads
752 to increases of soil moisture (Figure 12). The change in soil moisture content further affects the
753 partitioning of surface energy fluxes and the efficiency of the latent heat flux, thereby affecting
754 land surface temperature, as illustrated by Figure 11.

755 So far, we have been focusing on discussing the impacts of resolving dust mineralogy on winds
756 and precipitation relative to the HD27 control run. The large discrepancy in optical properties
757 between HD27 and mineral-resolved dust allows us to better understand how distinct dust
758 absorption impacts our climate through its distinct radiative effects.

759 As discussed in section 4.1, HD09 dust is nearly as scattering as mineral-resolved dust but exhibits
760 smaller regional variability. Section 5.1.2 shows that resolving dust mineralogy does not lead to
761 statistically significant anomalies on radiation relative to HD09. Consistently, there are no further
762 statistically significant impacts on winds (Figure 13c, d) and precipitation (Figure 13c, d).

763 To investigate the effectiveness of various dust scattering properties (e.g., HD27, HD09, BM) in
764 matching observations of precipitation rate, we compare the modeled precipitation with CRU TS
765 observations over the Sahara, Sahel and GC regions (Table 6). The greater difference between
766 HD09, BM and CRU (i.e., HD09 – CRU and BM – CRU) indicate that more scattering HD09 and
767 BM lead to a larger discrepancy between the modeled precipitation and CRU observations. In
768 contrast, Balkanski et al. (2021) describes the same balance of increased dust absorption and Sahel
769 precipitation but find improved agreement with Global Precipitation Climatology Project (GPCP)
770 data by assuming homogeneous dust containing 3% iron oxides by volume. Contrasts between that
771 study and ours result from differences between the GPCP and CRU data sets, contrasts in dust
772 absorption (related to contrasts in the dust size distribution or assumed index of refraction), non-
773 dust model biases in precipitation or differences between the slow response computed by
774 Balkanski et al. (2021) and the fast response that we calculate. The fast and slow response even

775 exhibit differences in the sign of the calculated precipitation anomaly within some regions of the
 776 WAM (Miller and Tegen, 1998; Jordan et al., 2018).

777 Table 6. Comparison of modeled precipitation rate (PRE, unit: mm/day) with observations from CRU TS
 778 dataset over 2001-2019 JJA. CRU column represents 19-year (2001-2019) JJA mean PRE over the region
 779 as well as 19-year standard deviation (std). HD27 – CRU column shows the 19-year mean PRE difference
 780 between HD27 control run and CRU observations, along with the corresponding std of this 19-year
 781 difference. Similar for HD09 – CRU and BM – CRU.

Comparison Region	CRU (mm/day)	HD27 – CRU (mm/day)	HD09 – CRU (mm/day)	BM – CRU (mm/day)
Sahara	0.08 ± 0.013	-0.03 ± 0.03	-0.03 ± 0.07	-0.04 ± 0.05
Sahel	2.99 ± 0.27	0.16 ± 0.56	-0.62 ± 0.43	-0.71 ± 0.41
Guinea Coast	6.16 ± 0.49	-0.28 ± 0.90	0.28 ± 1.02	0.64 ± 0.83

782

783 **6 Potential for reducing mineral tracers**

784 Thus far in this study, we have been using 45 mineral tracers in mineral-resolved experiments (i.e.,
 785 VOL, MG, and BM). However, it is important to investigate the potential of reducing the number
 786 of mineral tracers in climate models to lower computational costs. In this section, we take BM as
 787 a reference for providing the best comparisons with CRU temperature and CERES flux
 788 observations, and conduct an experiment named BM-RT to assess the possibility of reducing
 789 mineral tracers in BM. The BM-RT experiment consists of three sub-experiments, namely, BM-
 790 LC, BM-LCRH, and BM-LCRHRG. In each of the three sub-experiments, the number of mineral
 791 tracers is progressively reduced, allowing for an examination of the relative impacts of different
 792 minerals on climate compared to the reference BM.

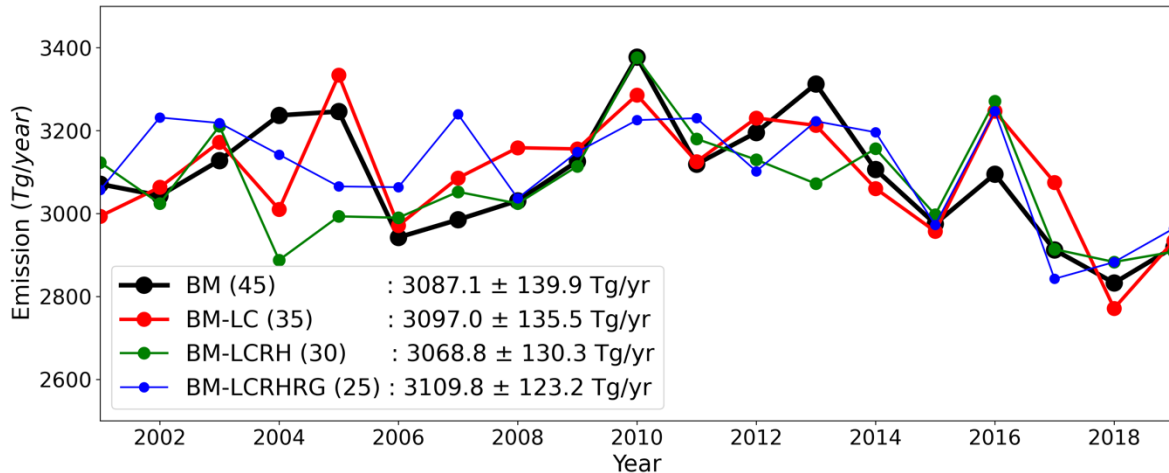
793 As discussed in section 4.1, the three clay minerals (i.e., illite, kaolinite, smectite) exhibit similar
 794 optical properties and perform similar functions in climate by hosting hematite. Hence, they can
 795 be combined in their interaction with radiation without significant impacts on climate. In addition,
 796 by lumping the three clay minerals together, the number of mineral tracers can be reduced from
 797 45 in BM (nine types of minerals \times five size bins) to 35 (seven types of minerals \times five size bins).

798 Therefore, in the first sub-experiment BM-LC (where ‘LC’ represents ‘Lump Clay minerals’), we
799 lump together the three clay minerals as one mineral species ‘clay433’.

800 Based upon the C1999 soil mineral composition that we use, externally mixed hematite is mainly
801 concentrated over the Sahel region (Ginoux et al. 2023, in preparation) and cannot be transported
802 to remote regions due to its high mass density. Obiso et al. (2023) shows that visible extinction
803 due to externally mixed hematite is negligible compared to other mineral components including
804 hematite internally mixed with other minerals. Thus, we further remove external hematite tracers
805 in the second sub-experiment BM-LCRH (where ‘RH’ indicates ‘Remove externally mixed
806 Hematite’). The mass fraction of external hematite is combined with internal hematite to ensure
807 that the total mineral fraction at emission remains equal to one. In this sub-experiment, the number
808 of mineral tracers is reduced from 35 in BM-LC to 30 in BM-LCRH.

809 Since there are no known specific impacts of gypsum on climate, we conducted the third sub-
810 experiment, BM-LCRHRG (‘RG’ indicates ‘Remove Gypsum’), where gypsum was removed. The
811 mass fraction previously attributed to gypsum at emission, which is very low at the global scale,
812 was proportionally redistributed among all other minerals. The number of mineral tracers is finally
813 reduced from 30 in BM-LCRH to 25 in BM-LCRHRG.

814 We analyze the 19-year (2001-2019) time series of total dust mineral emission before and after
815 reducing mineral tracers in Figure 15. We observe subtle differences in total mineral emission
816 between experiments, which arises from the feedback of mineral radiative interactions. However,
817 these differences are numerically small, and Student’s t-test suggests that the time series of the
818 four experiments are not statistically different. Additionally, the globally averaged DAOD and
819 SSA of each sub-experiment remains highly similar to those of the reference experiment BM, as
820 listed in Table 3.



821

822 Figure 15. Time series of total dust mineral emission from 2001 to 2019 before and after reducing the
 823 number of mineral tracers. The legend displays the following information: ‘Experiment name (number of
 824 mineral tracers): 19-year averaged total mineral emission ± 19-year standard deviation of total mineral
 825 emission’.

826 Given the highly similar optical properties of minerals before and after reducing mineral tracers,
 827 we further investigate their impact on climate. Firstly, we examine the clear-sky flux anomaly of
 828 each of the three sub-experiments at TOA and surface relative to the reference experiment BM, as
 829 shown in Supplementary Figure S14 for TOA and Supplementary Figure S15 for surface. We only
 830 observe a few statistically significant (p -value < 0.05) anomalies over the North Africa, suggesting
 831 that the reduction of mineral tracers in the three sub-experiments has a weak impact on radiation.

832 Furthermore, we investigate the anomaly in temperature profile, surface winds, and precipitation
 833 of each of the three sub-experiments relative to the reference experiment BM. The results are
 834 presented in Figure S16-S18 in the Supplement. No statistically significant (p -value < 0.05)
 835 temperature anomalies (Figure S16) and surface wind anomalies (Figure S17) is observed. Only a
 836 few statistically significant anomalies in precipitation are observed in the Supplementary Figure
 837 S18. These results suggest that the reduction of mineral tracers in the three sub-experiments has a
 838 weak impact on climate.

839 The results from the BM-RT experiment suggest combining clay minerals and excluding the
 840 externally mixed hematite and gypsum to simulate dust impact on radiation. This does not preclude
 841 similar conclusion for other impacts of dust on the Earth’s climate systems. The removal of mineral
 842 tracers reduces the number of mineral tracers from 45 to 25, effectively lowering computational
 843 costs without causing statistically significant impacts on simulating climate.

844 7 Conclusions

845 We simulate the distribution of dust mineralogy (i.e., illite, kaolinite, smectite, hematite, calcite,
846 feldspar, quartz, and gypsum) and activate their interaction with radiation in the GFDL AM4.0
847 model. Our investigation focuses on the radiative impacts of resolving dust mineralogy on Earth's
848 atmosphere and its fast response of land temperature, surface winds and precipitation.

849 We set up two baseline homogeneous dust control runs: HD27 and HD09, in which dust
850 mineralogy is considered as temporally and spatially uniform, the former following the standard
851 configuration for the dust optical properties in GFDL AM4.0 and the latter including a more
852 scattering dust. Three experiments with resolved mineralogy are also conducted: VOL, MG, and
853 BG, using three different mixing rules for the internal mixture between hematite and clay minerals
854 (i.e., volume weighted mean, Maxwell Garnett, and Bruggeman). The comparison of dust
855 absorption properties (e.g., SSA) with observation-based results suggests that the homogeneous
856 dust used in the standard GFDL AM4.0 (i.e., HD27) is overly absorptive, Maxwell Garnett and
857 Bruggeman mixing rules are more appropriate than volume weighted mixing rule in calculating
858 optical properties of internal mixtures of hematite and clays. Compared to HD27, the homogeneous
859 dust with reduced hematite content (HD09) and mineral-resolved dust (i.e., MG and BM) exhibit
860 much better agreement with AERONET retrievals and laboratory measurements in terms of dust
861 absorption properties (i.e., SSA). Additionally, resolving dust mineralogy enhances regional
862 variability in dust SSA compared to homogenous dust, further improves the agreement with
863 AERONET, even though it remains lower than the observed variability.

864 The two homogeneous dust control runs, HD27 and HD09, with distinct dust absorption properties,
865 allow us to investigate the impact of dust mineralogy on Earth's radiation and fast climate response
866 relative to distinct baseline homogeneous dust. In comparison to HD27, resolving mineralogy
867 reduces dust absorption. During JJA, the reduced dust absorption results in a reduction of over 50%
868 in NET downward radiation across the Sahara and approximately 20% over the Sahel at TOA.
869 Additionally, there is a reduction of around 25% in the atmospheric absorption of radiation over
870 the Sahara and around 10% over the Sahel in the atmosphere. The reduced surface absorption of
871 radiation by mineral-resolved dust leads to a temperature decrease of 0.66 K at the land surface
872 across the Sahara and an increase of 0.7 K over the Sahel. The reduced NET downward radiation
873 at TOA, attributed to the less absorption of radiation by mineral-resolved dust, suppresses ascent

874 and weakens the monsoon inflow from the Gulf of Guinea. This brings less moisture to the Sahel,
875 which combined with decreased ascent induces a reduction of precipitation. On the other hand,
876 compared to HD09, resolving dust mineralogy results in dust absorption comparable to that of
877 HD09 on a global scale. However, when resolving mineralogy, there is an increase in spatial
878 variation of dust absorption. Additionally, we observe a noticeable change in global distribution
879 of dust absorption, with more dust absorption distributed in the Southern Hemisphere and lower
880 dust absorption over Iceland and Taklamakan regions. Nevertheless, the higher spatial variation in
881 dust absorption does not lead to statistically significant changes in any of the climate aspects
882 mentioned above. The models with reduced absorption (HD09 and fully resolved mineralogy)
883 improve the comparison with observations of CERES fluxes and CRU land surface temperature.
884 We see a slightly better agreement with observations for fully resolved mineralogy than HD09
885 however it is not statistically significant. As such, when using fixed mineralogical composition,
886 we recommend using a 0.9% hematite content in volume, which represents the lowest of the three
887 hematite mixings considered by Balkanski et al. (2007).

888 Historically, climate models have relied on fixed refractive index to consider dust radiative forcing
889 starting (IPCC, 2001) with strongly absorptive value based on dust samples in Sahara (Patterson
890 et al., 1977) to more scattering values after dust absorption could be inferred from satellite and
891 surface observations (e.g., Sinyuk et al., 2003; Balkanski et al., 2007). With the launch of EMIT
892 in July 2022 and the expected delivery of a high-resolution map of soil mineralogy in source areas,
893 dust interactions with radiation in climate models will be calculated directly from the simulated
894 mineralogical composition (Li et al., 2021). Still, the additional burden of simulating a dozen
895 minerals may be too prohibitive for large ensemble climate models simulations. In such cases, our
896 analysis suggests the use of a fixed value providing similar radiative effects as the comprehensive
897 representation of minerals. However, our recommendation is directed toward the GFDL AM4.0
898 model with all its uncertainties related to mineral distribution, emission sources, and aerosol
899 transport. Moreover, incorporating dust mineralogy in models is likely to be important in other
900 aspects, such as cloud properties, ocean biogeochemistry, air quality and photochemistry. For
901 studies with resolved mineralogy, we show that the number of mineral tracers can be reduced from
902 45 to 25 without losing the quality of comparison with observations of CERES fluxes and CRU
903 surface temperature. Such reduction can be achieved by lumping together clay minerals, removing

904 external hematite and gypsum. For specific research such as biogeochemistry, it may be necessary
905 to fully resolve mineralogy to achieve accuracy.

906 This study has some limitations. First, the soil mineralogy map from C1999 is based on extensive
907 extrapolation and limited observations. In terms of the need to improve knowledge of soil
908 mineralogy in dust source regions, the launch in July 2022 of the EMIT instrument operating from
909 the International Space Station will provide mineral identifications of dust sources using
910 hyperspectral measurements (Green et al., 2020). The EMIT soil map measurements will improve
911 resolving dust mineralogy in climate models and advance our understanding of dust's effects in
912 the Earth system. Second, hematite and goethite are the most common iron oxides present in soils.
913 However, goethite is not considered in this study because not included in the used soil mineralogy
914 map. Previous studies suggest that goethite is generally more abundant than hematite, but it is less
915 absorptive than hematite in the visible spectrum (Formenti et al., 2014). Therefore, the abundance
916 of iron oxides may be underestimated in this study, which may lead to underestimation of dust
917 absorption in the SW. A more recent database by Journet et al. (2014) (J2014) includes the
918 distribution of goethite but it shares many limitations as C1999 (e.g., extensive extrapolation) and
919 has other major disadvantages, such as numbers of missing soil fractions of some minerals at some
920 locations. Third, the refractive index of hematite used in our study is close to the upper range of
921 the values available in literature (Zhang et al., 2015). Hence, the last two limitations,
922 underestimation of iron oxide content and overestimation of absorption by hematite, may have
923 compensating effects.

924 This study, by prescribing SST, calculates only the fast response to the dust DRE, without
925 including the slow response by the sea surface temperature. This avoids the need to spin-up the
926 model for decades before reaching new equilibrium but may overestimate the eventual response,
927 as shown by Miller and Tegen (1998) and Balkanski et al. (2021). This complicates model
928 evaluation because the observations include the slow response to dust. Variables like precipitation
929 are especially sensitive to the inclusion of the slow response because prescribed SST experiments
930 omit the surface energy balance over the ocean. Thus, the surface DRE beneath the aerosol layer,
931 which is generally negative, is not fully balanced by a fast reduction of evaporation (Miller et al.,
932 2004a). The addition of the surface balance in the slow response can reverse the sign of the fast
933 precipitation anomaly (Miller and Tegen, 1998; Jordan et al., 2018). In this study, the increase of
934 dust scattering (e.g., through consideration of dust mineral composition) generally reduces model

935 biases for all variables except precipitation. Future works may include satellite-based inventory of
936 soil mineralogy using fully coupled Earth's system components.

937 **8 Competing interests**

938 The contact author has declared that none of the authors has any competing interests.

939 **9 Acknowledgement**

940 This research is supported by a collaboration between Princeton University and NOAA GFDL,
941 Cooperative Institute for Modeling the Earth System (CIMES). A portion of this work is funded
942 by the Earth Surface Mineral Dust Source Investigation (EMIT), a NASA Earth Ventures-
943 Instrument (EVI-4) Mission. Carlos Pérez García-Pando and María Gonçalves Ageitos
944 acknowledge support from the European Research Council (ERC) under the Horizon 2020
945 research and innovation program through the ERC Consolidator Grant FRAGMENT (grant
946 agreement no. 773051), the AXA Research Fund through the AXA Chair on Sand and Dust Storms
947 at the Barcelona Supercomputing Center (BSC), the European Union's Horizon 2020 research and
948 innovation program under grant agreement no. 821205 (FORCeS) and the Department of Research
949 and Universities of the Government of Catalonia via the Research Group Atmospheric
950 Composition (code 2021 SGR 01550). Vincenzo Obiso was supported by the NASA Postdoctoral
951 Program at the NASA Goddard Institute for Space Studies administered by Oak Ridge Associated
952 Universities under contract with NASA (80HQTR21CA005). We acknowledge the CERES EBAF
953 Ed 4.2 data, which were obtained from the NASA Langley Research Center CERES ordering tool
954 at <https://ceres.larc.nasa.gov/data/>.

955

956 **10 References**

- 957 Allen, M. R. and Ingram, W. J.: Constrains on future changes in climate and the hydrologic cycle,
958 419, 224–232, 2002.
- 959 Atkinson, J. D., Murray, B. J., Woodhouse, M. T., Whale, T. F., Baustian, K. J., Carslaw, K. S.,
960 Dobbie, S., O’Sullivan, D., and Malkin, T. L.: The importance of feldspar for ice nucleation by
961 mineral dust in mixed-phase clouds, *Nature*, 498, 355–358, <https://doi.org/10.1038/nature12278>,
962 2013.
- 963 Balkanski, Y., Schulz, M., Claquin, T., and Guibert, S.: Reevaluation of Mineral aerosol radiative
964 forcings suggests a better agreement with satellite and AERONET data, *Atmos. Chem. Phys.*, 7,
965 81–95, <https://doi.org/DOI.10.5194/acp-7-81-2007>, 2007.
- 966 Balkanski, Y., Bonnet, R., Boucher, O., Checa-Garcia, R., and Servonnat, J.: Better representation
967 of dust can improve climate models with too weak an African monsoon, *Atmos. Chem. Phys.*, 21,
968 11423–11435, <https://doi.org/10.5194/acp-21-11423-2021>, 2021.
- 969 Di Biagio, C., Formenti, P., Balkanski, Y., Caponi, L., Cazaunau, M., Pangui, E., Journet, E.,
970 Nowak, S., Caquineau, S., Andreae O, M., Kandler, K., Saeed, T., Piketh, S., Seibert, D., Williams,
971 E., and Doussin, J. F. C.: Global scale variability of the mineral dust long-wave refractive index:
972 A new dataset of in situ measurements for climate modeling and remote sensing, *Atmos. Chem.*
973 *Phys.*, 17, 1901–1929, <https://doi.org/10.5194/acp-17-1901-2017>, 2017.
- 974 Di Biagio, C., Formenti, P., Balkanski, Y., Caponi, L., Cazaunau, M., Pangui, E., Journet, E.,
975 Nowak, S., Andreae, M. O., Kandler, K., Saeed, T., Piketh, S., Seibert, D., Williams, E., and
976 Doussin, J. F.: Complex refractive indices and single-scattering albedo of global dust aerosols in
977 the shortwave spectrum and relationship to size and iron content, *Atmos. Chem. Phys.*, 19, 15503–
978 15531, <https://doi.org/10.5194/acp-19-15503-2019>, 2019.
- 979 Bian, H. and Zender, C. S.: Mineral dust and global tropospheric chemistry: Relative roles of
980 photolysis and heterogeneous uptake, *J. Geophys. Res. Atmos.*, 108,
981 <https://doi.org/10.1029/2002jd003143>, 2003.
- 982 Bullard, J. E., Harrison, S. P., Baddock, M. C., Drake, N., Gill, T. E., McTainsh, G., and Sun, Y.:
983 Preferential dust sources: A geomorphological classification designed for use in global dust-cycle

984 models, *J. Geophys. Res. Earth Surf.*, 116, <https://doi.org/10.1029/2011JF002061>, 2011.

985 Chatziparaschos, M., Daskalakis, N., Myriokefalitakis, S., Kalivitis, N., Nenes, A., Goncalves
986 Ageitos, M., Costa-Sueros, M., Perez Garcia-Pando, C., Zanolli, M., Vrekoussis, M., and Kanakidou,
987 M.: Role of K-feldspar and quartz in global ice nucleation by mineral dust in mixed-phase clouds,
988 *Atmos. Chem. Phys.*, 23, 1785–1801, <https://doi.org/10.5194/acp-23-1785-2023>, 2023.

989 Claquin, T., SCHULZ, M., BALKANSKI, Y., and BOUCHER, O.: Uncertainties in assessing
990 radiative forcing by mineral dust, *Tellus B*, 50, 491–505, <https://doi.org/10.1034/j.1600->
991 0889.1998.t01-2-00007.x, 1998.

992 Claquin, T., Schulz, M., and Balkanski, Y. J.: Modeling the mineralogy of atmospheric dust
993 sources, *J. Geophys. Res. Atmos.*, 104, 22243–22256, <https://doi.org/10.1029/1999JD900416>,
994 1999.

995 Delworth, T. L., Broccoli, A. J., Rosati, A., Stouffer, R. J., Balaji, V., Beesley, J. A., Cooke, W.
996 F., Dixon, K. W., Dunne, J., Dunne, K. A., Durachta, J. W., Findell, K. L., Ginoux, P.,
997 Gnanadesikan, A., Gordon, C. T., Griffies, S. M., Gudgel, R., Harrison, M. J., Held, I. M., Hemler,
998 R. S., Horowitz, L. W., Klein, S. A., Knutson, T. R., Kushner, P. J., Langenhorst, A. R., Lee, H.
999 C., Lin, S. J., Lu, J., Malyshev, S. L., Milly, P. C. D., Ramaswamy, V., Russell, J., Schwarzkopf,
1000 M. D., Shevliakova, E., Sirutis, J. J., Spelman, M. J., Stern, W. F., Winton, M., Wittenberg, A. T.,
1001 Wyman, B., Zeng, F., and Zhang, R.: GFDL’s CM2 global coupled climate models. Part I:
1002 Formulation and simulation characteristics, *J. Clim.*, 19, 643–674,
1003 <https://doi.org/10.1175/JCLI3629.1>, 2006.

1004 Dentener, F. J., Carmichael, G. R., Zhang, Y., Lelieveld, J., and Crutzen, P. J.: Role of mineral
1005 aerosol as a reactive surface in the global troposphere, *J. Geophys. Res. Atmos.*, 101, 22869–22889,
1006 <https://doi.org/10.1029/96jd01818>, 1996.

1007 Donner, L. J., Wyman, B. L., Hemler, R. S., Horowitz, L. W., Ming, Y., Zhao, M., Golaz, J. C.,
1008 Ginoux, P., Lin, S. J., Schwarzkopf, M. D., Austin, J., Alaka, G., Cooke, W. F., Delworth, T. L.,
1009 Freidenreich, S. M., Gordon, C. T., Griffies, S. M., Held, I. M., Hurlin, W. J., Klein, S. A., Knutson,
1010 T. R., Langenhorst, A. R., Lee, H. C., Lin, Y., Magi, B. I., Malyshev, S. L., Milly, P. C. D., Naik,
1011 V., Nath, M. J., Pincus, R., Ploshay, J. J., Ramaswamy, V., Seman, C. J., Shevliakova, E., Sirutis,
1012 J. J., Stern, W. F., Stouffer, R. J., Wilson, R. J., Winton, M., Wittenberg, A. T., and Zeng, F.: The

1013 dynamical core, physical parameterizations, and basic simulation characteristics of the
1014 atmospheric component AM3 of the GFDL global coupled model CM3, *J. Clim.*, 24, 3484–3519,
1015 <https://doi.org/10.1175/2011JCLI3955.1>, 2011.

1016 Dubovik, O., Holben, B., Eck, T. F., Smirnov, A., Kaufman, Y. J., King, M. D., Tanre, D., and
1017 Slutsker, I.: Variability of absorption and optical properties of key aerosol types observed in
1018 worldwide locations, *J. Atmos. Sci.*, 59, 590–608, [https://doi.org/Doi 10.1175/1520-](https://doi.org/Doi%2010.1175/1520-0469(2002)059<0590:V0aaop>2.0.Co;2)
1019 [0469\(2002\)059<0590:V0aaop>2.0.Co;2](https://doi.org/Doi%2010.1175/1520-0469(2002)059<0590:V0aaop>2.0.Co;2), 2002.

1020 Dunne, J. P., Horowitz, L. W., Adcroft, A. J., Ginoux, P., Held, I. M., John, J. G., Krasting, J. P.,
1021 Malyshev, S., Naik, V., Paulot, F., Shevliakova, E., Stock, C. A., Zadeh, N., Balaji, V., Blanton,
1022 C., Dunne, K. A., Dupuis, C., Durachta, J., Dussin, R., Gauthier, P. P. G., Griffies, S. M., Guo, H.,
1023 Hallberg, R. W., Harrison, M., He, J., Hurlin, W., McHugh, C., Menzel, R., Milly, P. C. D.,
1024 Nikonov, S., Paynter, D. J., Ploshay, J., Radhakrishnan, A., Rand, K., Reichl, B. G., Robinson, T.,
1025 Schwarzkopf, D. M., Sentman, L. T., Underwood, S., Vahlenkamp, H., Winton, M., Wittenberg,
1026 A. T., Wyman, B., Zeng, Y., and Zhao, M.: The GFDL Earth System Model Version 4.1 (GFDL-
1027 ESM 4.1): Overall Coupled Model Description and Simulation Characteristics, *J. Adv. Model.*
1028 *Earth Syst.*, 12, <https://doi.org/10.1029/2019MS002015>, 2020.

1029 Evans, S., Malyshev, S., Ginoux, P., and Shevliakova, E.: The Impacts of the Dust Radiative Effect
1030 on Vegetation Growth in the Sahel, *Global Biogeochem. Cycles*, 33, 1582–1593,
1031 <https://doi.org/10.1029/2018GB006128>, 2019.

1032 Formenti, P., Caquineau, S., Chevaillier, S., Klaver, A., Desboeufs, K., Rajot, J. L., Belin, S., and
1033 Briois, V.: Dominance of goethite over hematite in iron oxides of mineral dust from Western
1034 Africa: Quantitative partitioning by X-ray absorption spectroscopy, *J. Geophys. Res. Atmos.*, 119,
1035 12,740–12,754, <https://doi.org/10.1002/2014JD021668>, 2014.

1036 Gates, W. L.: AMIP: the Atmospheric Model Intercomparison Project, *Bull. - Am. Meteorol. Soc.*,
1037 73, 1962–1970, [https://doi.org/10.1175/1520-0477\(1992\)073<1962:ATAMIP>2.0.CO;2](https://doi.org/10.1175/1520-0477(1992)073<1962:ATAMIP>2.0.CO;2), 1992.

1038 Giles, D. M., Sinyuk, A., Sorokin, M. G., Schafer, J. S., Smirnov, A., Slutsker, I., Eck, T. F.,
1039 Holben, B. N., Lewis, J. R., Campbell, J. R., Welton, E. J., Korkin, S. V., and Lyapustin, A. I.:
1040 Advancements in the Aerosol Robotic Network (AERONET) Version 3 database - Automated
1041 near-real-time quality control algorithm with improved cloud screening for Sun photometer

1042 aerosol optical depth (AOD) measurements, *Atmos. Meas. Tech.*, 12, 169–209,
1043 <https://doi.org/10.5194/amt-12-169-2019>, 2019.

1044 Ginoux, P.: Effects of nonsphericity on mineral dust modeling, *J. Geophys. Res. Atmos.*, 108,
1045 <https://doi.org/10.1029/2002jd002516>, 2003.

1046 Ginoux, P., Chin, M., Tegen, I., Prospero, J. M., Holben, B., Dubovik, O., and Lin, S. J.: Sources
1047 and distributions of dust aerosols simulated with the GOCART model, *J. Geophys. Res.*, 106,
1048 20255–20273, <https://doi.org/10.1029/2000jd000053>, 2001.

1049 Gliß, J., Mortier, A., Schulz, M., Andrews, E., Balkanski, Y., Bauer, S. E., Benedictow, A. M. K.,
1050 Bian, H., Checa-Garcia, R., Chin, M., Ginoux, P., Griesfeller, J. J., Heckel, A., Kipling, Z.,
1051 Kirkevåg, A., Kokkola, H., Laj, P., Le Sager, P., Tronstad Lund, M., Lund Myhre, C., Matsui, H.,
1052 Myhre, G., Neubauer, D., Van Noije, T., North, P., Olivié, D. J. L., Rémy, S., Sogacheva, L.,
1053 Takemura, T., Tsigaridis, K., and Tsyro, S. G.: AeroCom phase III multi-model evaluation of the
1054 aerosol life cycle and optical properties using ground- And space-based remote sensing as well as
1055 surface in situ observations, *Atmos. Chem. Phys.*, 21, 87–128, [https://doi.org/10.5194/acp-21-87-](https://doi.org/10.5194/acp-21-87-2021)
1056 2021, 2021.

1057 Gonçalves Ageitos, M., Obiso, V., Miller, R. L., Jorba, O., Klose, M., Dawson, M., Balkanski, Y.,
1058 Perlwitz, J., Basart, S., Di Tomaso, E., Escribano, J., MacChia, F., Montané, G., Mahowald, N.
1059 M., Green, R. O., Thompson, D. R., and Pérez García-Pando, C.: Modeling dust mineralogical
1060 composition: sensitivity to soil mineralogy atlases and their expected climate impacts, *Atmos.*
1061 *Chem. Phys.*, 23, 8623–8657, <https://doi.org/10.5194/acp-23-8623-2023>, 2023.

1062 Green, R. O., Mahowald, N., Ung, C., Thompson, D. R., Bator, L., Bennet, M., Bernas, M.,
1063 Blackway, N., Bradley, C., Cha, J., Clark, P., Clark, R., Cloud, D., Diaz, E., Ben Dor, E., Duren,
1064 R., Eastwood, M., Ehlmann, B. L., Fuentes, L., Ginoux, P., Gross, J., He, Y., Kalashnikova, O.,
1065 Kert, W., Keymeulen, D., Klimesh, M., Ku, D., Kwong-Fu, H., Liggett, E., Li, L., Lundeen, S.,
1066 Makowski, M. D., Mazer, A., Miller, R., Mouroulis, P., Oaida, B., Okin, G. S., Ortega, A., Oyake,
1067 A., Nguyen, H., Pace, T., Painter, T. H., Pempejian, J., Garcia-Pando, C. P., Pham, T., Phillips, B.,
1068 Pollock, R., Purcell, R., Realmuto, V., Schoolcraft, J., Sen, A., Shin, S., Shaw, L., Soriano, M.,
1069 Swayze, G., Thingvold, E., Vaid, A., and Zan, J.: The Earth Surface Mineral Dust Source
1070 Investigation: An Earth Science Imaging Spectroscopy Mission, in: 2020 IEEE Aerospace
1071 Conference, 1–15, <https://doi.org/10.1109/AERO47225.2020.9172731>, 2020.

1072 Grider, A., Ponette-González, A., and Heindel, R.: Calcium and ammonium now control the pH
1073 of wet and bulk deposition in Ohio, U.S., *Atmos. Environ.*, 310,
1074 <https://doi.org/10.1016/j.atmosenv.2023.119986>, 2023.

1075 Guo, H., Ming, Y., Fan, S., Zhou, L., Harris, L., and Zhao, M.: Two-Moment Bulk Cloud
1076 Microphysics With Prognostic Precipitation in GFDL's Atmosphere Model AM4.0: Configuration
1077 and Performance, *J. Adv. Model. Earth Syst.*, 13, <https://doi.org/10.1029/2020MS002453>, 2021.

1078 Harris, I., Osborn, T. J., Jones, P., and Lister, D.: Version 4 of the CRU TS monthly high-resolution
1079 gridded multivariate climate dataset, *Sci. Data*, 7, <https://doi.org/10.1038/s41597-020-0453-3>,
1080 2020.

1081 Harrison, A. D., Lever, K., Sanchez-Marroquin, A., Holden, M. A., Whale, T. F., Tarn, M. D.,
1082 McQuaid, J. B., and Murray, B. J.: The ice-nucleating ability of quartz immersed in water and its
1083 atmospheric importance compared to K-feldspar, *Atmos. Chem. Phys.*, 19, 11343–11361,
1084 <https://doi.org/10.5194/acp-19-11343-2019>, 2019.

1085 Huang, Y., Kok, J. F., Saito, M., and Muñoz, O.: Single-scattering properties of ellipsoidal dust
1086 aerosols constrained by measured dust shape distributions, *Atmos. Chem. Phys.*, 23, 2557–2577,
1087 <https://doi.org/10.5194/acp-23-2557-2023>, 2023.

1088 Huneus, N., Schulz, M., Balkanski, Y., Griesfeller, J., Prospero, J., Kinne, S., Bauer, S., Boucher,
1089 O., Chin, M., Dentener, F., Diehl, T., Easter, R., Fillmore, D., Ghan, S., Ginoux, P., Grini, A.,
1090 Horowitz, L., Koch, D., Krol, M. C., Landing, W., Liu, X., Mahowald, N., Miller, R., Morcrette,
1091 J. J., Myhre, G., Penner, J., Perlwitz, J., Stier, P., Takemura, T., and Zender, C. S.: Global dust
1092 model intercomparison in AeroCom phase i, *Atmos. Chem. Phys.*, 11, 7781–7816,
1093 <https://doi.org/10.5194/acp-11-7781-2011>, 2011.

1094 Jin, Q., Yang, Z. L., and Wei, J.: High sensitivity of Indian summer monsoon to Middle East dust
1095 absorptive properties, *Sci. Rep.*, 6, <https://doi.org/10.1038/srep30690>, 2016.

1096 Jordan, A. K., Gnanadesikan, A., and Zaitchik, B.: Simulated dust aerosol impacts on western
1097 sahelian rainfall: Importance of ocean coupling, *J. Clim.*, 31, 9107–9124,
1098 <https://doi.org/10.1175/JCLI-D-17-0819.1>, 2018.

1099 Journet, E., Balkanski, Y., and Harrison, S. P.: A new data set of soil mineralogy for dust-cycle
1100 modeling, *Atmos. Chem. Phys.*, 14, 3801–3816, <https://doi.org/10.5194/acp-14-3801-2014>, 2014.

1101 Kandler, K., Schutz, L., Deutscher, C., Ebert, M., Hofmann, H., Jackel, S., Jaenicke, R., Knippertz,
1102 P., Lieke, K., Massling, A., Petzold, A., Schladitz, A., Weinzierl, B., Wiedensohler, A., Zorn, S.,
1103 and Weinbruch, S.: Size distribution, mass concentration, chemical and mineralogical composition
1104 and derived optical parameters of the boundary layer aerosol at Tinfou, Morocco, during SAMUM
1105 2006, *Tellus Ser. B-Chemical Phys. Meteorol.*, 61, 32–50, <https://doi.org/10.1111/j.1600->
1106 0889.2008.00385.x, 2009.

1107 Kelly, J. T., Chuang, C. C., and Wexler, A. S.: Influence of dust composition on cloud droplet
1108 formation, *Atmos. Environ.*, 41, 2904–2916, <https://doi.org/10.1016/j.atmosenv.2006.12.008>,
1109 2007.

1110 Kok, J. F.: A scaling theory for the size distribution of emitted dust aerosols suggests climate
1111 models underestimate the size of the global dust cycle, *Proc. Natl. Acad. Sci. U. S. A.*, 108, 1016–
1112 1021, <https://doi.org/10.1073/pnas.1014798108>, 2011.

1113 Kok, J. F., Ridley, D. A., Zhou, Q., Miller, R. L., Zhao, C., Heald, C. L., Ward, D. S., Albani, S.,
1114 and Haustein, K.: Smaller desert dust cooling effect estimated from analysis of dust size and
1115 abundance, *Nat. Geosci.*, 10, 274–278, <https://doi.org/10.1038/Ngeo2912>, 2017.

1116 Kok, J. F., Adebisi, A. A., Albani, S., Balkanski, Y., Checa-Garcia, R., Chin, M., Colarco, P. R.,
1117 Hamilton, D. S., Huang, Y., Ito, A., Klose, M., Leung, D. M., Li, L., Mahowald, N. M., Miller, R.
1118 L., Obiso, V., Pérez García-Pando, C., Rocha-Lima, A., Wan, J. S., and Whicker, C. A.: Improved
1119 representation of the global dust cycle using observational constraints on dust properties and
1120 abundance, *Atmos. Chem. Phys.*, 21, 8127–8167, <https://doi.org/10.5194/acp-21-8127-2021>, 2021.

1121 Lau, K. M., Kim, K. M., Sud, Y. C., and Walker, G. K.: A GCM study of the response of the
1122 atmospheric water cycle of West Africa and the Atlantic to Saharan dust radiative forcing, *Ann.*
1123 *Geophys.*, 27, 4023–4037, <https://doi.org/10.5194/angeo-27-4023-2009>, 2009.

1124 Li, L., Mahowald, N. M., Miller, R. L., Pérez García-Pando, C., Klose, M., Hamilton, D. S.,
1125 Gonçalves Ageitos, M., Ginoux, P., Balkanski, Y., Green, R. O., Kalashnikova, O., Kok, J. F.,
1126 Obiso, V., Paynter, D., and Thompson, D. R.: Quantifying the range of the dust direct radiative
1127 effect due to source mineralogy uncertainty, *Atmos. Chem. Phys.*, 21, 3973–4005,
1128 <https://doi.org/10.5194/acp-21-3973-2021>, 2021.

1129 Liu, Y. and Daum, P. H.: Relationship of refractive index to mass density and self-consistency of

1130 mixing rules for multicomponent mixtures like ambient aerosols, *J. Aerosol Sci.*, 39, 974–986,
1131 <https://doi.org/10.1016/j.jaerosci.2008.06.006>, 2008.

1132 Loeb, N. G., Doelling, D. R., Wang, H., Su, W., Nguyen, C., Corbett, J. G., Liang, L., Mitrescu,
1133 C., Rose, F. G., and Kato, S.: Clouds and the Earth’S Radiant Energy System (CERES) Energy
1134 Balanced and Filled (EBAF) top-of-atmosphere (TOA) edition-4.0 data product, *J. Clim.*, 31, 895–
1135 918, <https://doi.org/10.1175/JCLI-D-17-0208.1>, 2018.

1136 Mahowald, N.: Aerosol indirect effect on biogeochemical cycles and climate, *Science (80-.)*, 334,
1137 794–796, <https://doi.org/10.1126/science.1207374>, 2011.

1138 Markel, V. A.: Introduction to the Maxwell Garnett approximation: tutorial, *J. Opt. Soc. Am. A*,
1139 33, 1244, <https://doi.org/10.1364/josaa.33.001244>, 2016.

1140 Matthes, K., Funke, B., Andersson, M. E., Barnard, L., Beer, J., Charbonneau, P., Clilverd, M. A.,
1141 Dudok De Wit, T., Haberreiter, M., Hendry, A., Jackman, C. H., Kretzschmar, M., Kruschke, T.,
1142 Kunze, M., Langematz, U., Marsh, D. R., Maycock, A. C., Misios, S., Rodger, C. J., Scaife, A. A.,
1143 Seppälä, A., Shangguan, M., Sinnhuber, M., Tourpali, K., Usoskin, I., Van De Kamp, M.,
1144 Verronen, P. T., and Versick, S.: Solar forcing for CMIP6 (v3.2), *Geosci. Model Dev.*, 10, 2247–
1145 2302, <https://doi.org/10.5194/gmd-10-2247-2017>, 2017.

1146 Meinshausen, M., Vogel, E., Nauels, A., Lorbacher, K., Meinshausen, N., Etheridge, D. M., Fraser,
1147 P. J., Montzka, S. A., Rayner, P. J., Trudinger, C. M., Krummel, P. B., Beyerle, U., Canadell, J.
1148 G., Daniel, J. S., Enting, I. G., Law, R. M., Lunder, C. R., O’Doherty, S., Prinn, R. G., Reimann,
1149 S., Rubino, M., Velders, G. J. M., Vollmer, M. K., Wang, R. H. J., and Weiss, R.: Historical
1150 greenhouse gas concentrations for climate modelling (CMIP6), *Geosci. Model Dev.*, 10, 2057–
1151 2116, <https://doi.org/10.5194/gmd-10-2057-2017>, 2017.

1152 Miller, R. L. and Tegen, I.: Climate response to soil dust aerosols, *J. Clim.*, 11, 3247–3267,
1153 [https://doi.org/10.1175/1520-0442\(1998\)011<3247:CRTSDA>2.0.CO;2](https://doi.org/10.1175/1520-0442(1998)011<3247:CRTSDA>2.0.CO;2), 1998.

1154 Miller, R. L. and Tegen, I.: Radiative Forcing of a Tropical Direct Circulation by Soil Dust
1155 Aerosols, *J. Atmos. Sci.*, 56, 2403–2433, [https://doi.org/10.1175/1520-0469\(1999\)056<2403:RFOATD>2.0.CO;2](https://doi.org/10.1175/1520-0469(1999)056<2403:RFOATD>2.0.CO;2), 1999.

1157 Miller, R. L., Perlwitz, J., and Tegen, I.: Feedback upon dust emission by dust radiative forcing
1158 through the planetary boundary layer, *J. Geophys. Res. D Atmos.*, 109, 1–17,

1159 <https://doi.org/10.1029/2004JD004912>, 2004a.

1160 Miller, R. L., Perlwitz, J., and Tegen, I.: Modeling Arabian dust mobilization during the Asian
1161 summer monsoon: The effect of prescribed versus calculated SST, *Geophys. Res. Lett.*, 31, 1–4,
1162 <https://doi.org/10.1029/2004GL020669>, 2004b.

1163 Miller, R. L., Knippertz, P., Pérez García-Pando, C., Perlwitz, J. P., and Tegen, I.: Impact of dust
1164 radiative forcing upon climate, in: *Mineral Dust: A Key Player in the Earth System*, Springer
1165 Netherlands, 327–357, https://doi.org/10.1007/978-94-017-8978-3_13, 2014.

1166 Ming, Y., Ramaswamy, V., and Persad, G.: Two opposing effects of absorbing aerosols on global-
1167 mean precipitation, *Geophys. Res. Lett.*, 37, <https://doi.org/10.1029/2010GL042895>, 2010.

1168 Obiso, V., Gonçalves Ageitos, M., Pérez García-Pando, C., Schuster, G. L., Bauer, S. E., Biagio,
1169 C. Di, Formenti, P., Perlwitz, J. P., Tsigaridis, K., and Miller, R. L.: Observationally constrained
1170 regional variations of shortwave absorption by iron oxides emphasize the cooling effect of dust,
1171 <https://doi.org/10.5194/egusphere-2023-1166>, 2023.

1172 Panta, A., Kandler, K., Alastuey, A., González-Flórez, C., González-Romero, A., Klose, M.,
1173 Querol, X., Reche, C., Yus-Díez, J., and Pérez García-Pando, C.: Insights into the single-particle
1174 composition, size, mixing state, and aspect ratio of freshly emitted mineral dust from field
1175 measurements in the Moroccan Sahara using electron microscopy, *Atmos. Chem. Phys.*, 23, 3861–
1176 3885, <https://doi.org/10.5194/acp-23-3861-2023>, 2023.

1177 Patterson, E. M., Gillette, D. A., and Stockton, B. H.: Complex index of refraction between 300
1178 and 700 nm for Saharan aerosols, *J. Geophys. Res.*, 82, 3153–3160,
1179 <https://doi.org/10.1029/jc082i021p03153>, 1977.

1180 Paulot, F., Ginoux, P., Cooke, W. F., Donner, L. J., Fan, S., Lin, M. Y., Mao, J., Naik, V., and
1181 Horowitz, L. W.: Sensitivity of nitrate aerosols to ammonia emissions and to nitrate chemistry:
1182 Implications for present and future nitrate optical depth, *Atmos. Chem. Phys.*, 16, 1459–1477,
1183 <https://doi.org/10.5194/acp-16-1459-2016>, 2016.

1184 Pérez, C., Nickovic, S., Pejanovic, G., Baldasano, J. M., and Özsoy, E.: Interactive dust-radiation
1185 modeling: A step to improve weather forecasts, *J. Geophys. Res. Atmos.*, 111,
1186 <https://doi.org/10.1029/2005JD006717>, 2006.

1187 Perez Garcia-Pando, C., Miller, R. L., Perlwitz, J. P., Rodríguez, S., and Prospero, J. M.:

1188 Predicting the mineral composition of dust aerosols: Insights from elemental composition
1189 measured at the Izaña Observatory, *Geophys. Res. Lett.*, 43, 10,520–10,529,
1190 <https://doi.org/10.1002/2016GL069873>, 2016.

1191 Perlwitz, J. P., Pérez García-Pando, C., and Miller, R. L.: Predicting the mineral composition of
1192 dust aerosols - Part 1: Representing key processes, *Atmos. Chem. Phys.*, 15, 11593–11627,
1193 <https://doi.org/10.5194/acp-15-11593-2015>, 2015a.

1194 Perlwitz, J. P., Pérez García-Pando, C., and Miller, R. L.: Predicting the mineral composition of
1195 dust aerosols - Part 2: Model evaluation and identification of key processes with observations,
1196 *Atmos. Chem. Phys.*, 15, 11629–11652, <https://doi.org/10.5194/acp-15-11629-2015>, 2015b.

1197 Persad, G. G., Ming, Y., and Ramaswamy, V.: The role of aerosol absorption in driving clear-sky
1198 solar dimming over East Asia, *J. Geophys. Res.*, 119, 10,410–10,424,
1199 <https://doi.org/10.1002/2014JD021577>, 2014.

1200 Réveillet, M., Dumont, M., Gascoïn, S., Lafaysse, M., Nabat, P., Ribes, A., Nheili, R., Tuzet, F.,
1201 Ménégot, M., Morin, S., Picard, G., and Ginoux, P.: Black carbon and dust alter the response of
1202 mountain snow cover under climate change, *Nat. Commun.*, 13, [https://doi.org/10.1038/s41467-](https://doi.org/10.1038/s41467-022-32501-y)
1203 022-32501-y, 2022.

1204 Rosenfeld, D., Rudich, Y., and Lahav, R.: Desert dust suppressing precipitation: A possible
1205 desertification feedback loop, *Proc. Natl. Acad. Sci. U. S. A.*, 98, 5975–5980,
1206 <https://doi.org/10.1073/pnas.101122798>, 2001.

1207 Ryder, C. L., Marengo, F., Brooke, J. K., Estelles, V., Cotton, R., Formenti, P., McQuaid, J. B.,
1208 Price, H. C., Liu, D., Ausset, P., Rosenberg, P. D., Taylor, J. W., Choularton, T., Bower, K., Coe,
1209 H., Gallagher, M., Crosier, J., Lloyd, G., Highwood, E. J., and Murray, B. J.: Coarse-mode mineral
1210 dust size distributions, composition and optical properties from AER-D aircraft measurements
1211 over the tropical eastern Atlantic, *Atmos. Chem. Phys.*, 18, 17225–17257,
1212 <https://doi.org/10.5194/acp-18-17225-2018>, 2018.

1213 Samset, B. H.: Aerosol absorption has an underappreciated role in historical precipitation change,
1214 *Commun. Earth Environ.*, 3, <https://doi.org/10.1038/s43247-022-00576-6>, 2022.

1215 Scanza, R. A., Mahowald, N., Ghan, S., Zender, C. S., Kok, J. F., Liu, X., Zhang, Y., and Albani,
1216 S.: Modeling dust as component minerals in the Community Atmosphere Model: Development of

1217 framework and impact on radiative forcing, *Atmos. Chem. Phys.*, 15, 537–561,
1218 <https://doi.org/10.5194/acp-15-537-2015>, 2015.

1219 Schuster, G. L., Dubovik, O., and Arola, A.: Remote sensing of soot carbon - Part 1: Distinguishing
1220 different absorbing aerosol species, *Atmos. Chem. Phys.*, 16, 1565–1585,
1221 <https://doi.org/10.5194/acp-16-1565-2016>, 2016.

1222 Sinyuk, A., Torres, O., and Dubovik, O.: Combined use of satellite and surface observations to
1223 infer the imaginary part of refractive index of Saharan dust, *Geophys. Res. Lett.*, 30,
1224 <https://doi.org/10.1029/2002GL016189>, 2003.

1225 Sinyuk, A., Sinyuk, A., Holben, B. N., Eck, T. F., Eck, T. F., M. Giles, D., M. Giles, D., Slutsker,
1226 I., Slutsker, I., Korokin, S., Korokin, S., S. Schafer, J., S. Schafer, J., Smirnov, A., Smirnov, A.,
1227 Sorokin, M., Sorokin, M., and Lyapustin, A.: The AERONET Version 3 aerosol retrieval algorithm,
1228 associated uncertainties and comparisons to Version 2, *Atmos. Meas. Tech.*, 13, 3375–3411,
1229 <https://doi.org/10.5194/amt-13-3375-2020>, 2020.

1230 Skiles, S. M. K., Flanner, M., Cook, J. M., Dumont, M., and Painter, T. H.: Radiative forcing by
1231 light-absorbing particles in snow, <https://doi.org/10.1038/s41558-018-0296-5>, 1 November 2018.

1232 Sokolik, I. N. and Toon, O. B.: Incorporation of mineralogical composition into models of the
1233 radiative properties of mineral aerosol from UV to IR wavelengths, *J. Geophys. Res.*, 104, 9423–
1234 9444, <https://doi.org/10.1029/1998jd200048>, 1999.

1235 Song, C. H. and Carmichael, G. R.: Gas-particle partitioning of nitric acid modulated by alkaline
1236 aerosol, *J. Atmos. Chem.*, 40, 1–22, <https://doi.org/10.1023/A:1010657929716>, 2001.

1237 Song, Q., Zhang, Z., Yu, H., Kok, J. F., Di Biagio, C., Albani, S., Zheng, J., and Ding, J.: Size-
1238 resolved dust direct radiative effect efficiency derived from satellite observations, *Atmos. Chem.*
1239 *Phys.*, 22, 13115–13135, <https://doi.org/10.5194/acp-22-13115-2022>, 2022.

1240 Stephens, G. L., Wood, N. B., and Pakula, L. A.: On the radiative effects of dust on tropical
1241 convection, *Geophys. Res. Lett.*, 31, 1–4, <https://doi.org/10.1029/2004GL021342>, 2004.

1242 Strong, J. D. O., Vecchi, G. A., and Ginoux, P.: The response of the tropical Atlantic and West
1243 African climate to Saharan dust in a fully coupled GCM, *J. Clim.*, 28, 7071–7092,
1244 <https://doi.org/10.1175/JCLI-D-14-00797.1>, 2015.

1245 Taylor, K. E., Williamson, D., and Zwiers, F.: The sea surface temperature and sea-ice
1246 concentration boundary conditions for AMIP II simulations, Program for Climate Model
1247 Diagnosis and Intercomparison, Lawrence Livermore ..., 2000.

1248 Wu, C., Lin, Z., and Liu, X.: The global dust cycle and uncertainty in CMIP5 (Coupled Model
1249 Intercomparison Project phase 5) models, *Atmos. Chem. Phys.*, 20, 10401–10425,
1250 <https://doi.org/10.5194/acp-20-10401-2020>, 2020.

1251 Zender, C. S., Newman, D., and Torres, O.: Spatial heterogeneity in aeolian erodibility: Uniform,
1252 topographic, geomorphic, and hydrologic hypotheses, *J. Geophys. Res. Atmos.*, 108,
1253 <https://doi.org/10.1029/2002jd003039>, 2003.

1254 Zhang, X. L., Wu, G. J., Zhang, C. L., Xu, T. L., and Zhou, Q. Q.: What is the real role of iron
1255 oxides in the optical properties of dust aerosols?, *Atmos. Chem. Phys.*, 15, 12159–12177,
1256 <https://doi.org/10.5194/acp-15-12159-2015>, 2015.

1257 Zhao, A., Ryder, C. L., and Wilcox, L. J.: How well do the CMIP6 models simulate dust aerosols?,
1258 *Atmos. Chem. Phys.*, 22, 2095–2119, <https://doi.org/10.5194/acp-22-2095-2022>, 2022.

1259 Zhao, M., Golaz, J. C., Held, I. M., Guo, H., Balaji, V., Benson, R., Chen, J. H., Chen, X., Donner,
1260 L. J., Dunne, J. P., Dunne, K., Durachta, J., Fan, S. M., Freidenreich, S. M., Garner, S. T., Ginoux,
1261 P., Harris, L. M., Horowitz, L. W., Krasting, J. P., Langenhorst, A. R., Liang, Z., Lin, P., Lin, S.
1262 J., Malyshev, S. L., Mason, E., Milly, P. C. D., Ming, Y., Naik, V., Paulot, F., Paynter, D., Phillipps,
1263 P., Radhakrishnan, A., Ramaswamy, V., Robinson, T., Schwarzkopf, D., Seman, C. J.,
1264 Shevliakova, E., Shen, Z., Shin, H., Silvers, L. G., Wilson, J. R., Winton, M., Wittenberg, A. T.,
1265 Wyman, B., and Xiang, B.: The GFDL Global Atmosphere and Land Model AM4.0/LM4.0: 1.
1266 Simulation Characteristics With Prescribed SSTs, *J. Adv. Model. Earth Syst.*, 10, 691–734,
1267 <https://doi.org/10.1002/2017MS001208>, 2018a.

1268 Zhao, M., Golaz, J. C., Held, I. M., Guo, H., Balaji, V., Benson, R., Chen, J. H., Chen, X., Donner,
1269 L. J., Dunne, J. P., Dunne, K., Durachta, J., Fan, S. M., Freidenreich, S. M., Garner, S. T., Ginoux,
1270 P., Harris, L. M., Horowitz, L. W., Krasting, J. P., Langenhorst, A. R., Liang, Z., Lin, P., Lin, S.
1271 J., Malyshev, S. L., Mason, E., Milly, P. C. D., Ming, Y., Naik, V., Paulot, F., Paynter, D., Phillipps,
1272 P., Radhakrishnan, A., Ramaswamy, V., Robinson, T., Schwarzkopf, D., Seman, C. J.,
1273 Shevliakova, E., Shen, Z., Shin, H., Silvers, L. G., Wilson, J. R., Winton, M., Wittenberg, A. T.,

1274 Wyman, B., and Xiang, B.: The GFDL Global Atmosphere and Land Model AM4.0/LM4.0: 2.
1275 Model Description, Sensitivity Studies, and Tuning Strategies, *J. Adv. Model. Earth Syst.*, 10,
1276 735–769, <https://doi.org/10.1002/2017MS001209>, 2018b.

1277 Paul Ginoux, María Gonçalves Ageitos, Qianqian Song, Ronald L Miller, Vincenzo Obiso, and
1278 Carlos Pérez García-Pando (2023), Implementation of dust mineralogy in the GFDL AM4.0
1279 climate model, in preparation.

1280 IPCC 2001, *Climate Change 2001: The Scientific Basis, Summary for Policy Makers and*
1281 *Technical Summary of the Working Group 1 Report*, Intergovernmental Panel on Climate Change,
1282 edited by: Houghton, J. T., Ding, Y., Griggs, D. J., Noguer, M., van der Linden, P. J., and Xiaosu,
1283 D., Cambridge University Press, Cambridge, UK, 2001.

1284